# PHOTOANODE AND COUNTER ELECTRODE MODIFICATION FOR MORE EFFICIENT DYE SENSITIZED SOLAR CELLS

by

YICHEN ZHENG

B.S., Zhejiang Gongshang University, 2011

A THESIS

submitted in partial fulfillment of the requirements for the degree

MASTER OF SCIENCE

Department of Chemistry
College of Arts and Sciences

KANSAS STATE UNIVERSITY
Manhattan, Kansas

2014

Approved by:

Major Professor
Jun Li

# Copyright

# Abstract

With the increasing consumption of energy and the depletion of fossil fuels, finding an alternative energy source is critical. Solar energy is one of the most promising energy sources and solar cells are the devices that convert solar radiation into electricity. Currently, the most widely used solar cell is based on p-n junction formed with crystalline silicon materials. While showing high efficiency, the high fabrication cost limits its broad applications. Dye sensitized solar cell (DSSC) is a promising low-cost alternative to the Si solar cell, but its efficiency is much lower. Improvements in materials and interfaces are needed to increase the DSSC efficiency while maintain the low cost. In this thesis, three projects were investigated to optimize the DSSC efficiency and reduce the cost. The first project is to optimize the $TiO_2$ barrier layers on Fluorine-doped Tin Dioxide (FTO) surface. Two preparation methods, i.e. $TiCl_4$ solution treatment and thermal oxidation of sputtered Ti metal films, were employed and systematically studied in order to minimize electron-hole recombination and electron backflow during photovoltaic processes of DSSCs. $TiCl_4$ solution treatment method was found to create a porous $TiO_2$ barrier layer. Ti sputtering method created a very compact $TiO_2$ blocking layer. Two methods showed different characteristics and may be used for different DSSC studies. The second project is to reduce the DSSC cost while maintaining the efficiency by replacing the expensive Pt counter electrode with a novel vertically aligned carbon nanofiber (VACNF) electrode. A large specific electrode surface area (~125 $cm^2$ over 1 $cm^2$ geometric area) was obtained by using VACNFs. The relatively high surface area, good electric conductivity and the large numbers of active graphitic edges existed in cone-like microstructure of VACNFs were employed to improve redox reaction rate of $I_3^-/I^-$ mediators in the electrolyte. Faster electron transfer and good catalytic activities were obtained with such counter electrodes. The third project is to develop a metal organic chemical vapor deposition (MOCVD) method to coat $TiO_2$ shells on VACNF arrays as potential photoanodes in the DSSC system in order to improve the electron transfer. Fabrication processes were demonstrated and preliminary materials were characterized with scanning electron microscopy and transmission electron microscopy. MOCVD at 300 mTorr vapor pressure at 550° C for 120 min was found to be the optimal condition.

# Table of Contents

# List of Figures

# List of Schematics

# Acknowledgements

I would like to thank my parents, Ping Li and Qikan Zheng, for letting me stand on their shoulders. I want to thank my wife, Ye Wang, who has her faith in me. I thank Dr. Jun Li for advising me through these years patiently. I also want to thank all my group members, Yiqun Yang, Steven Klankowski, Luxi Swisher, Foram Madiyar, Emery Brown, and all my friends in my life.

# Chapter 1 - Introduction

## Motivation

For 21st century, environmental and energy issue has become one of the critical problems that need to be solved. During the past decades, the economic crises and the short of fossil fuels have driven the development to utilize new energy sources that are clean and powerful. The most promising and commendable source is the solar energy from the sun, which is very powerful and can be used permanently.

## Solar Cells

In order to harvest the solar energy from sun, a photovoltaic device that converts solar energy into electrical energy is needed. This photovoltaic device, also named as solar cell, can capture the photons in the sun light and convert them into electron flux in the system. Extensive studies have been done to investigate the solar cell systems, which have evolved in three generations.

**Figure 1.1 Images of three generations of solar cells. (left) the first generation solar cell, (middle) the second generation solar cell, (right) the third generation solar cell.**

The first-generation solar cell is the most common type of solar cell, which mainly consists of the silicon-based solar cells. They have a high efficiency, but also a high cost. In order to further increase the cell efficiency, instead of single junction, multi-junction structure solar cells have been studied and utilized. Figure 1.2 shows that the cells using multi-junction structure can reach up to 44% efficiency with a three-junction structure. However, the price is also doubled or tripled to build a multi-junction solar cell. Nowadays, the first generation solar

cells are mostly used for the military and outer space activities because of the high expense. The other problem of silicon-based solar is the Shockley-Queisser theoretical limit, which limits the maximum efficiency to be 32%, due to their single p-n junction structure. Even though multi-junction solar cells can achieve higher efficiency than 32%, their cost is much too expensive as mentioned.

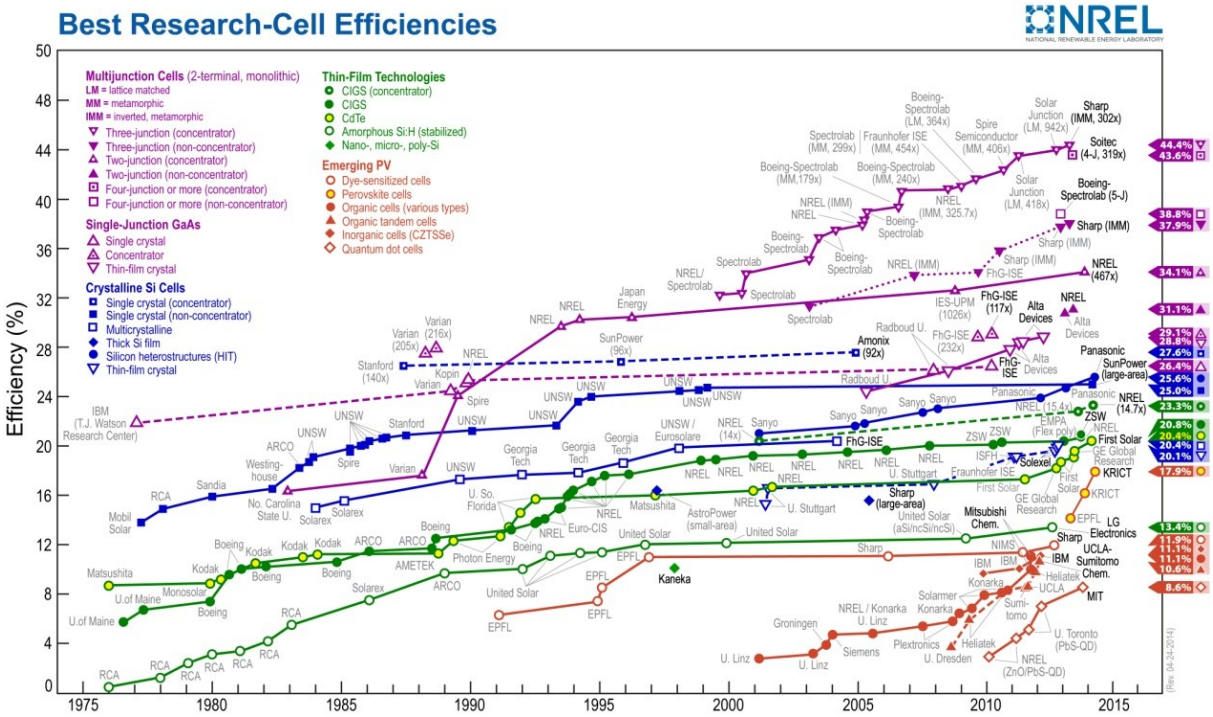


**Figure 1.2 Best efficiencies obtained for research solar cells since 1975 (Copyright © 2014 NREL)**

In order to reduce the cost of the solar cells so that they can be more broadly used, the second generation of solar cells was invented by using thin film technology. Cost is lowered by reducing the thickness of the cell from couple hundreds of micrometers down to just several micrometers, which reduces the use of materials. For example, single crystalline Si based solar cell needs hundreds of micrometers to completely absorb the incident light, and it is very expensive to build such thick single crystalline Si layer. The amorphous Si based solar cell, as one of the second generation solar cells, only needs several micrometers to completely absorb the light. However, reducing the thickness leads lower energy conversion efficiency, which is one of the problems of the second generation solar cells. But it is very attractive due to its low cost. The solar cells that we commonly use today are mostly the second generation. Their

average efficiency is around 10%, such as CIGS (Copper Indium Gallium Selenide) thin film solar cell, CdTe (Cadmium Telluride) thin film solar cell, amorphous Si thin film solar cell, etc. , which are listed in Figure 1.2. They work well for small power applications but do not meet the requirements as large-scale power sources.

The third generation consists of a family of emerging solar cells, which have total different structures and working principles from the 1st and 2nd generations. The examples include organic cells[1-5], polymer cells[6, 7], organic tandem cells[8-11], dye sensitized solar cells (DSSCs)[12-18], etc.[1, 12, 13, 19-21] as shown in Figure 1.2.

Figure 1.2 shows the best efficiencies from research solar cells till 2014. The highest efficiency is 44.4%, which was obtained using a three-junction tandem solar cell, which belongs to the first generation. The single junction solar cell with single crystalline Si has an efficiency of 27.6%, which is getting closer to the Shockley-Queisser theoretical limit. The mostly widely used second generation solar cell is based on amorphous Si, which has an efficiency of 13.4%. The emerging solar cells, such as Dye-sensitized solar cells, have a lower efficiency than the first and second generation solar cells, but it is very promising, and it attracts many attentions.

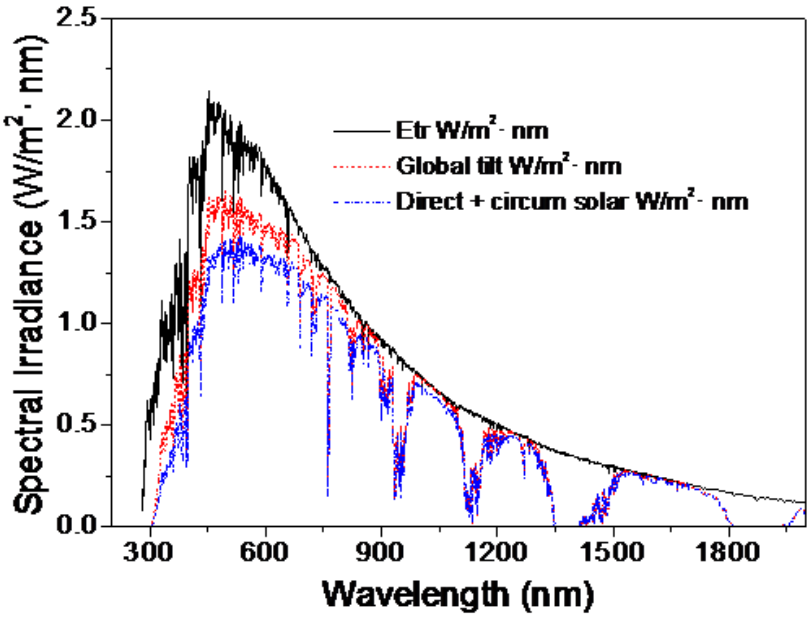

**Figure 1.3 The standard solar spectrum. (from an online source: http://rredc.nrel.gov/solar/spectra/am1.5/ASTMG173/ASTMG173.html). The 1 sun AM1.5G standard is represented by the red curve**

Figure 1.3 shows the standard solar spectrum, which includes three curves. The black solid curve stands for the extraterrestrial radiation, which means the solar spectrum of the solar radiation at the top of atmosphere at a mean Earth-Sun distance. The red dotted curve stands for the solar spectral radiation from solar disk plus sky diffuse and diffuse reflected from ground with a solar zenith angle of 48.19 degree. The blue dash curve stands for the sum direct normal irradiance and spectral irradiance. Direct normal irradiance means nearly parallel (0.5 degree divergent cone) radiation on surface with surface normal pointing to the sun, excluding scattered sky and reflected ground radiation. The Spectral irradiance mean, the irradiance within 5 degree diameter field of view centered on the 0.5 degree diameter solar disk, but excluding the radiation from the disk. The solar spectrum in red dotted curve is used as the AM 1.5G standard solar spectrum in most solar cell studies, and it is also used as the standard solar spectrum in my studies.

## Dye-Sensitized Solar Cells (DSSCs)

Among the 3rd generation solar cells, Dye-Sensitized Solar Cell is one of the most promising solar energy harvesting devices, and a lot works have been done to investigate the DSSCs since it was invented by Michael Gratzel 20 years ago. Now the Gratzel cell (DSSCs) can reach an efficiency of about 12%.[12, 13]

### *Structure of DSSCs*

The structure of a DSSC differs greatly from that of a 2nd generation silicon-based cell. As shown in Scheme 1, a basic DSSC consists of 2 different electrodes, one is photoanode, and the other one is a counter electrode. For the photoanode, transparent conducing oxide (TCO) coated glass is normally used as a substrate. A layer of $TiO_2$ semiconductor nanoparticle network is deposited on the top of the TCO coated substrate. Dye molecules (for example, N-719 (Di-tetrabutylammonium cis-bis(isothiocyanato)bis(2,2'-bipyridyl-4,4'-dicarboxylato)ruthenium (II)), which are the sensitizers that absorb light, are adsorbed on the $TiO_2$ nanoparticle surface. For the

counter electrode, a Pt coated TCO substrate is usually used. Between photo anode and counter electrode, an electrolyte containing $I_3^-/I^-$ redox couple is filled and serves as mediators for hole transport and regeneration of the excited dye molecules.

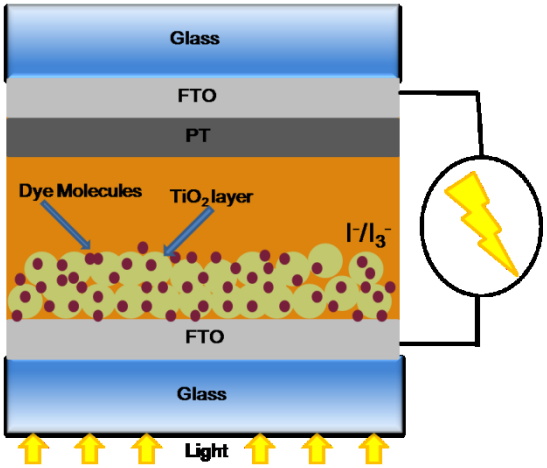


**Scheme 1. Components and structure of a traditional $TiO_2$ nanoparticle based dye sensitized solar cell.**

### *Principles of DSSCs*

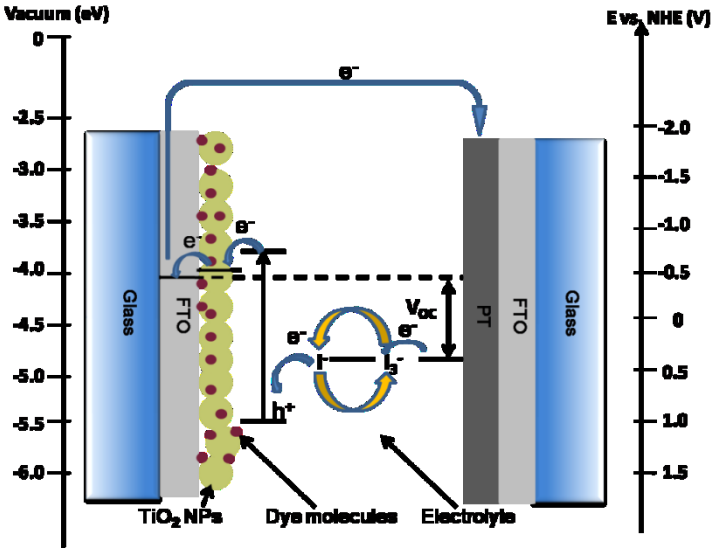


**Scheme 2. Energy level diagram and electron transfer principles in the traditional $TiO_2$ nanoparticle based DSSC system.**

Scheme 2 shows the electron pathway in the DSSC system. When light irradiates on the photo anode, an electron from the dye is excited from ground state to its excited state. Because of

the downhill effect, the excited electron will be injected into $TiO_2$ layer, whose conduction band has a lower energy level than the LUMO energy level of the dye molecule. Then the electron will travel from $TiO_2$ to TCO substrate based on the same downhill effect. The electron then flows through the external circuit, generates electricity, and flows to Pt coated counter electrode. At the counter electrode, the electron reduces $I_3^-$ into $I^-$. $I^-$ then will arrive at the oxidized dye molecules on the photoanode, and the oxidized dye will be reduced by $I^-$, while $I^-$ will at the same time get oxidized into $I_3^-$. This completes a full circle without any net consumption so that the dye molecules are regenerated and the system can continuously generate electricity as long as there is light irradiation.

## Improvements to DSSCs

A lot of studies have been done to improve the performance of DSSCs and at the meantime to reduce the cost. Most studies fall into the following three categories: first, modification to photoanodes and counter electrodes. Photoanodes can be modified by using different $TiO_2$ structures [22-29] or different materials[30-32] to improve the electron transfer or light absorption. Counter electrodes can be modified by replacing Pt with other materials [33-42] to improve the electron transfer and catalytic activity. Second, the modifications to sensitizers[43-49] to improve the light absorption wavelength range. Third, improve the electrolyte for better hole transport and thermal stability.

In this thesis, on the photoanode part, a $TiO_2$ thin layer was studied, which was used as a barrier layer to prevent electrons from flowing back to electrolyte or recombining with holes left in dye molecules. By minimizing the electron leakage, an optimized photoanode for DSSC study can be obtained. On the counter electrode part, traditional Pt electrode was replaced by a new Vertically-aligned carbon nanofiber (VACNF) electrode, which has a lower cost and a comparable performance. The VACNF counter electrode has a much larger specific surface area and a larger amount of graphitic edges due to VACNF cone-like structure, which is beneficial for higher catalytic activities and fast reaction rates. At last, VACNF fabrication on FTO-coated quartz, Cu and Si substrates was demonstrated and a metal organic chemical vapor deposition (MOCVD) process was established to coat a $TiO_2$ layer on VACNFs grown on the three different substrates.

# Chapter 2 - Investigation of $TiO_2$ barrier Layer in DSSCs


## Abstract

A $TiO_2$ barrier layer is critical in enhancing the performance of dye-sensitized solar cells (DSSCs). Two methods to prepare $TiO_2$ barrier layers on Fluorine-doped Tin Dioxide (FTO) surface were systematically studied in order to minimize electron-hole recombination and electron backflow during photovoltaic processes of DSSCs. The film structure and materials properties were correlated with the photovoltaic characteristics and electrochemical properties. In the first approach, a porous $TiO_2$ layer was deposited by wet chemical treatment of the sample with $TiCl_4$ solutions for time periods varying from 0 to 60 minutes. The N719 dye molecules were found to be able to insert into the porous barrier layers. The 20-min treatment formed a non-uniform but intact $TiO_2$ layer of ~100 to 300 nm in thickness, which gave the highest open-circuit voltage $V_{OC}$, short-circuit photocurrent density $J_{SC}$, and energy conversion efficiency. But thicker $TiO_2$ barrier layers caused decrease in $J_{SC}$, possibly limited by poor electron transport. In the second approach, a compact $TiO_2$ barrier layer was created by sputter-coating 0 to 15 nm Ti on FTO/glass and then oxidizing it with thermal treatment at 500° C in the air for 30 min. The dye molecules were found to only attach at the outer surface of the barrier layer with little change versus the thickness. These two kinds of barrier layer showed different characteristics and may be used for different DSSC studies.


## Introduction

Dye Sensitized Solar Cells[50] (DSSCs) have attracted great attention in recent decades due to the low cost, high sustainability and fairly high power conversion efficiency (> 10%). A high-efficient DSSC requires assembling different functional materials and optimizing their interfaces for achieving the best performance in all processes including photon capture, charge separation, electron/hole transport, and dye regeneration. One of the critical interfaces lies between the transparent conductive oxide (TCO) electrode and the mesoporous $TiO_2$ nanoparticle film. Studies indicated that depositing a proper $TiO_2$ barrier layer of 10s to 100s nm between the TCO and the mesoporous $TiO_2$ nanoparticle film can significantly improve the solar cell efficiency.[51-59] This barrier layer helps to improve the adhesion of $TiO_2$ nanoparticles on the TCO surface and blocks TCO electrode from direct contact with electrolyte. It is essential in minimizing

electron backflow from TCO electrode into the electrolyte and suppressing electron-hole recombination at the TCO surface. The role of the barrier layer was found increasingly important at low light intensities,[58, 59] and in solid-state DSSCs involving Ohmic hole-transport media[60-62].

So far the explored methods to build $TiO_2$ barrier layer include so-gel processes[51, 56, 63], $TiCl_4$ solution treatment[54, 57, 58], vacuum sputtering deposition of $TiO_2$[52], and vacuum sputtering deposition of Ti metal followed by conversion into $TiO_2$ by acid treatment[53] or thermal oxidation[55]. The effects of the barrier layer were evaluated by comparing the performance of traditional DSSCs of microns thick $TiO_2$ nanoparticle film with and without the barrier layer. In general, a compact $TiO_2$ layer was found to be effective in lowering the electron loss at the TCO/electrolyte interface, increasing the shunt resistance, and therefore increasing the fill factor and overall cell efficiency.[58, 59] However, the function of the barrier layer was mixed with other components of the whole DSSCs and was not easily extracted from the full cell characterization. Here we report a study of DSSCs fabricated with the $TiO_2$ barrier layer as the sole semiconductor layer in the photoanode. The structure, photovoltaic and electrochemical properties of the $TiO_2$ barrier layers prepared by two methods, i.e. $TiCl_4$ solution treatment and thermal oxidation conversion of sputter-coated Ti metal films, were systematically studied at varied thickness with and without dye sensitization. Since it avoided the overwhelming contribution from the thick mesoporous $TiO_2$ film, the measured photoelectron transport, back reactions, and charge recombination can be directly correlated with the materials properties of the barrier layer. This study provides a method for optimizing the TCO/$TiO_2$ interface in DSSC fabrication and serve as a thin-film DSSC platform for investigating photovoltaic properties macromolecular sensitizers (such as photosynthesis complexes) which are not easily to access the interior surface of traditional mesoporous $TiO_2$ nanoparticle films.[64]

## Experimental

**Preparation of Photoanode of DSSC**. Commercial fluorine-doped tin oxide (FTO) glass (Pilkington Glass, Lathrop, CA) was used as the photoanode substrate, which was first cleaned by sonication in isopropanol, ethanol and acetone each for 15 min. In the second step, some FTO anodes were treated with 40 mM $TiCl_4$ solution, which is made by adding 99.9% $TiCl_4$ solution into deionized water, at 70℃ in oil bath with varied time from 5 to 60 min. while others were

sputter-coated with a uniform Ti film at the thickness of 5, 10, and 15 nm, respectively, using a high-resolution ion beam coater (Model No. 681, Gatan Inc., Pleasanton, CA). Third, after the $TiCl_4$ treatment or Ti sputtering, the photoanodes were annealed in tube furnace open to the air at 500℃ for 30 min. This improved the crystallinity of the solution-deposited $TiO_2$ and converted the Ti metal into $TiO_2$ by thermal oxidation[65], respectively. Finally, the annealed anodes were immersed in a 0.5 mM *cis*-diisothiocyanato-bis(2,2'-bipyridyl-4,4'-dicarboxylato) ruthenium(II) bis(tetrabutylammonium) (N-719 dye, shown in Figure A6) in dried ethanol solution (Solaronix, Aubonne, Switzerland) for 12 h for dye adsorption on the $TiO_2$ surface. The samples were rinsed with dried ethanol to remove physisorbed dyes.

**Preparation of Cathode of DSSC**. Two 1 mm diameter holes were drilled at the diagonal corners of the 1 $cm^2$ optical window of the FTO-coated glass, and then the FTO/glass was sputtered with 25 nm thick Pt using the above ion beam coater. The Pt sputtered cathode was annealed at 450℃ in the air for activation.

**Assembly and Characterization of DSSCs**. The anode and cathode were bonded through a 60 μm thick hot melt spacer (Solaronix, Aubonne, Switzerland) following our previous procedure.[66] Then the Iodolyte AN-50 electrolyte (Solaronix, Aubonne, Switzerland) consisting of 50 mM triiodide, 0.1 M LiI, and 0.5 M 1,2-dimethyl-3-propylimidazolium iodide in acetonitrile was filled in the cell by a syringe. The assembled cell with an active area of 1 cm × 1 cm was characterized under one sun illumination with a 300 W Xe lamp solar simulator and an AM 1.5G filter (Newport, Irvine, CA) to obtain the photocurrent-voltage (I-V) curve, and the dynamic responses of short-circuit current ($J_{SC}$) and open-circuit voltage ($V_{OC}$). Incident Photon-to-Current Efficiency (IPCE) curves were measured with a 75 W Xe lamp and a monochromator (74004, Oriel Instrument, Newport, Irvine, CA).

**Electrochemical and Materials Characterization**. Cyclic voltammetry was carried out with a potentiostat (CHI 440A, CH Instruments,Austin, TX) in an acetonitrile solution containing 0.1 M $LiClO_4$ using a three-electrode setup vs. a Pt counter electrode and a Ag/AgCl reference electrode (filled with acetonitrile solution containing 10 mM $AgNO_3$ in 1 M $LiClO_4$) to characterize the N719 dye adsorption and electrochemical activity. Scanning electron microscopy (SEM) was carried with a field-emission system (FEI Nano430). Raman spectra

were measured with a DXR Raman microscope (Thermo Electron, WI) using 50X objective, 530 nm laser, and 5 mW laser power.

## Results and Discussion

Incubating the photoanode in aqueous $TiCl_4$ solution before or after deposition of the $TiO_2$ nanocrystal film during DSSC fabrication has been used to form a $TiO_2$ thin film as the interfacial barrier layer [56, 58, 67] or the protecting layer [52, 62, 68, 69]. This method was adopted as the first approach for the study of interfacial barrier layers. As shown in Fig. A1, a DSSC cell with a ~5 μm thick film formed with sintered 20 nm dia. $TiO_2$ nanoparticles (NPs) subjected to the $TiCl_4$ treatment both before and after $TiO_2$ NP film deposition shows the highest $J_{SC}$, largest $V_{OC}$, and longest electron lifetime τ (as indicated by the $V_{OC}$ decay time constant after the light is switched off[56, 70]) which are consistent with literature.[56-58] The $TiO_2$ barrier layer is indeed critical in enhancing the DSSC performance. Since our focus here is on the understanding the properties of $TiO_2$ barrier layer formed on the FTO surface, the following studies were carried out using the photoanodes with only the $TiO_2$ barrier layer. The thick $TiO_2$ NP film was skipped so that the photovoltaic information are dominated by the TCO/electrolyte interface similar to the reports that more pronounced interfacial effects were observed at low light intensities.[58, 59]

The SEM images in Figures 2.1a-d show the change of the top-surface morphology of the FTO/glass photoanodes as the $TiCl_4$ treatment time was increased. The starting FTO/glass sample (Figure 2.1a) showed typical crystalline feature of ~200 to 400 nm in size. Such crystalline surface became fluffy as thicker $TiO_2$ layer was deposited by increasing $TiCl_4$ treatment time. Only the samples with 20, 40 and 60 min. treatment were shown because the change in the samples below 20 min. $TiCl_4$ treatment was too small to be observed. To get around with the large surface roughness of the FTO electrode and estimate the deposited $TiO_2$ thickness, a polished Si substrate was treated with the $TiCl_4$ for 20 min. following the similar procedure. Figure 2.1e shows the 45° perspective view SEM image and Figure 2.1f shows the cross-sectional view. The $TiO_2$ barrier layer is not uniform, with the thickness varying from ~100 nm in the thinnest region to ~300 nm at nucleation sites, but it clearly covers the whole surface. The overall thickness is comparable to the optimal thickness obtained with spray pyrolysis method on a solid-state DSSC by B. Peng et al.[62]

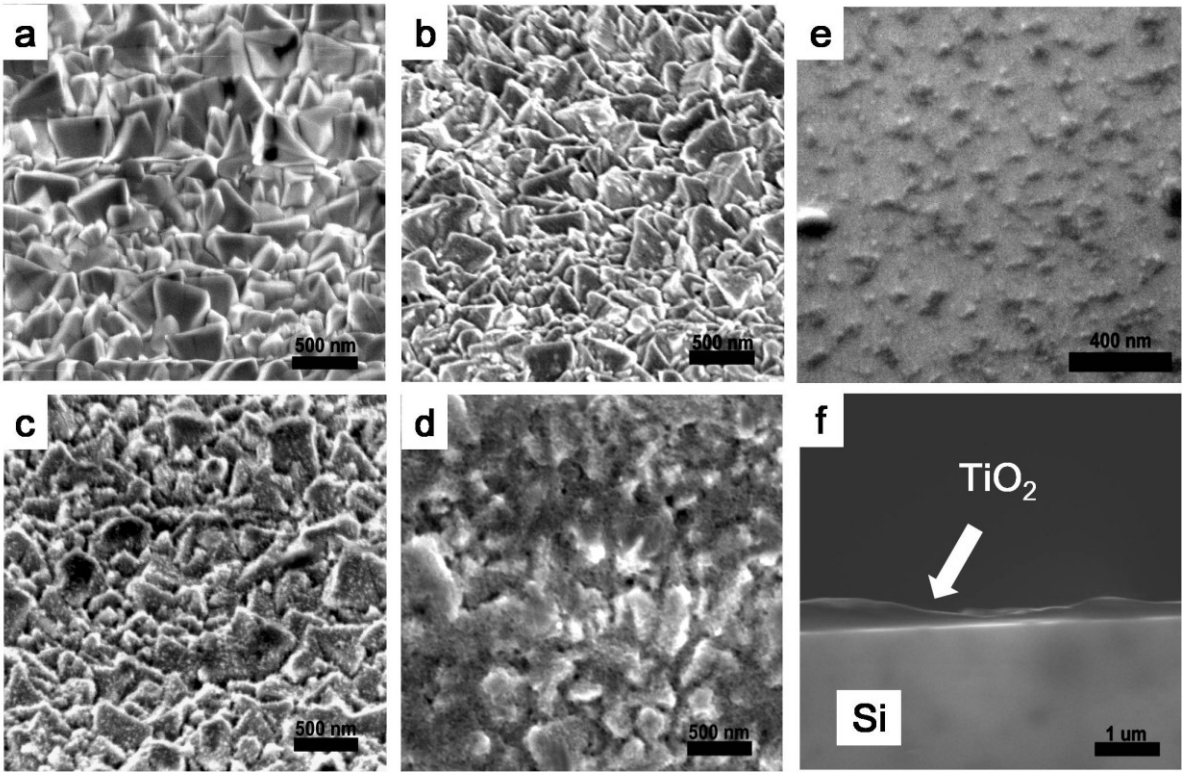


**Figure 2.1. SEM images at 45° perspective view of (a) bare FTO/glass surface and those after (b) 20 min., (c) 40 min., and (d) 60 min. of $TiCl_4$ treatment. (e) The 45° perspective view and (f) cross-sectional view SEM images of a 20 min. treated sample on a polished Si surface.**

The bare FTO/glass photoanodes and those after 5 to 60 minutes of $TiCl_4$ treatment were assembled into DSSCs following the standard procedure.[50, 66, 71] The characteristics of these DSSCs are shown in Figure 2.2. To understand the origin of the photocurrent, two sets of identical samples were compared. One set was directly used without applying any dye (Figures 2.2a-c) and another set was incubated in a N719 solution to adsorb a monolayer of dye (Figure 2.2d-f). Since anatase $TiO_2$ is a semiconductor material with a bandgap of ~3.2 V, it strongly absorbs UV light with wavelength below ~387 nm and generates a photocurrent. As a result, even the bare $TiO_2$/FTO/glass electrodes without dye adsorption showed clear photovoltaic properties. As the $TiCl_4$ treatment time was increased, both the $J_{SC}$ and $V_{OC}$ increased monotonically until reaching the maximum values with 20 min. treatment. However, the treatments longer than 20 min. tended to reduce $J_{SC}$ while maintaining the maximum value of

$V_{OC}$, indicating that the barrier layer still functioned well in blocking electron backflow but

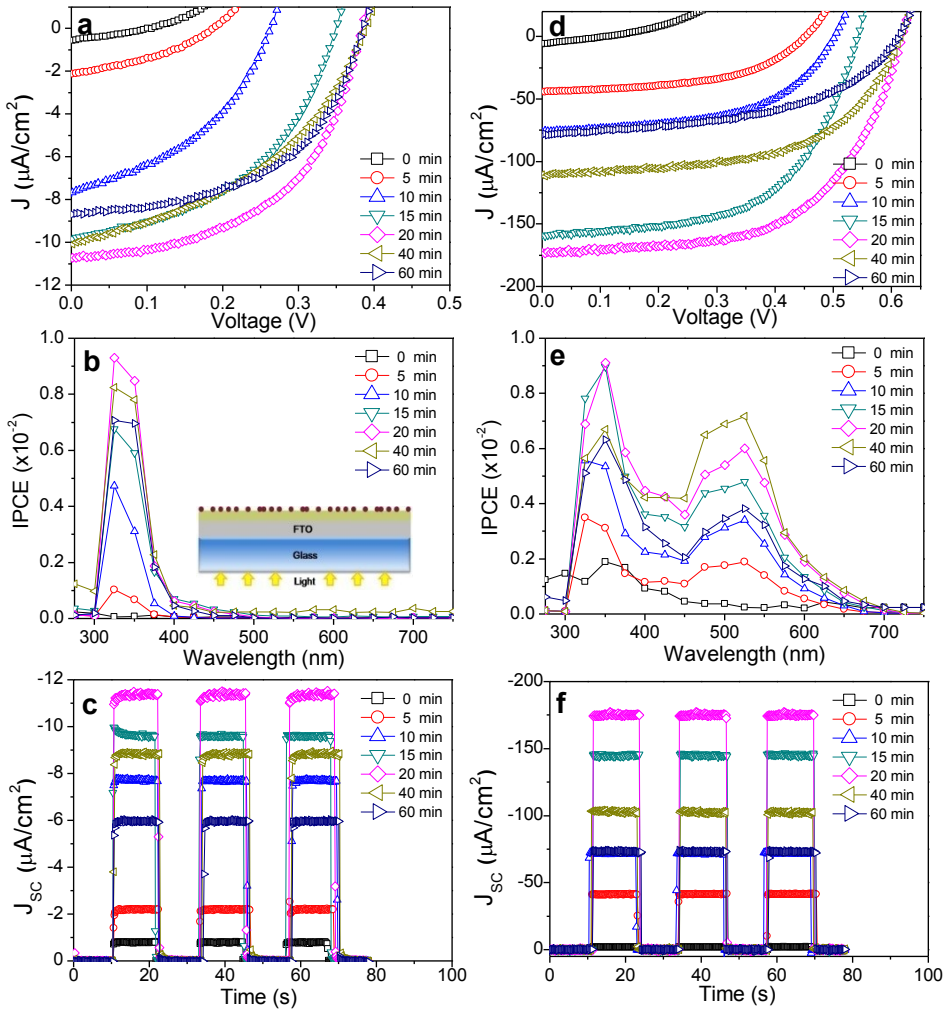


failed to collect photocurrent effectively.

**Figure 2.2. I-V curves (a and d), IPCE curves (b and e), and $J_{SC}$ responses during switching light on/off (c and f) of the DSSCs made of bare FTO photoanodes and those after $TiCl_4$ treatment for 5 to 60 minutes. Panels a-c were collected with the photoanodes without N719 dye adsorption while panels d-f were measured with samples after N719 dye adsorption.**

The photocurrent generation by the $TiO_2$ layer was further illustrated in the IPCE curves in Figure 2.2b. Clearly, the photocurrent was completely generated by the light below ~400 nm in wavelength. The IPCE value quickly increased when the wavelength was reduced below 387 nm

(at which photon energy is above the bandgap of anatase $TiO_2$ $E_g$ = ~3.2 eV) but then sharply dropped when the wavelength was further reduced below ~320 nm (3.87 eV), forming a high IPCE band around 320-360 nm. The IPCE cutoff below ~320 nm was due to the strong absorption by the glass substrate and FTO coating (with $E_g$ = ~3.6 eV for Tin oxide), which completely blocked the light from reaching the $TiO_2$ film. Hence the IPCE value in 320 to 360 nm range represents the photovoltaic properties of the $TiO_2$ overlayer. Figure 2.2c further shows that the dynamic response of $J_{SC}$ while the photo shutter was turned on and off. When the light was turned on, the $J_{SC}$ immediately jump to the maximum and stayed nearly constant afterward. When light was switched off, the current immediately drop to zero without any delay. The $TiO_2$ layer deposited by $TiCl_4$ treatment did not show any effects in slowing down the electron transfer rate. The $J_{SC}$ magnitude correlates well with the trend of I-V curves vs. different $TiCl_4$ treatment time in Figure 2.2a, which is maximum with 20 min. $TiCl_4$ treatment. The photocurrent was found to decrease as the $TiCl_4$ treatment time was increased to 40 and 60 min., presumably due to electron traps by impurities and defects in thicker $TiO_2$ barrier layer as reported by B. Peng et al.[62]

After incubating the $TiO_2$/FTO/glass in N719 solution, a monolayer of dye presumably formed on the $TiO_2$ surface similar to the general process in DSSC fabrication.[71] The value of $J_{SC}$ increased by ~10 to 15 times as shown in Figures 2.2d and 2.2f. Taking 20 min. treated samples as an example, the $J_{SC}$ is about 11 $\mu A/cm^2$ without dye (Figure 2.2a), but is ramped up to about 170 $\mu A/cm^2$ after dye adsorption (Figure 2.2d). Clearly, the dye molecule significantly enhanced the photocurrent generation. Similar to the bare $TiO_2$/FTO anode, both $J_{SC}$ and $V_{OC}$ initially increased vs. the $TiCl_4$ treatment time and reached the maximum with 20 min. treatment. With longer $TiCl_4$ treatment time, the $V_{OC}$ remained the same while the $J_{SC}$ value decreased. It is clear that 20 min. treatment is optimum in forming an effective $TiO_2$ barrier layer to minimize the electron backflow to the electrolyte while suppressing its recombination with holes (oxidized dye or triiodide). However, thicker $TiO_2$ coating apparently affected electron transfer and adversely decreased the electron collection efficiency.

The IPCE curves in Figure 2.2e show a broad peak around 525 nm in wavelength in addition to the $TiO_2$ peaks around 320-360 nm, which is attributed to the photon capture by N719 dye. The magnitude of the IPCE peak corresponding to the dye molecules is in concert

with that of the $TiO_2$ barrier layer as the $TiCl_4$ treatment time is varied, both reaching the maximum with 20 to 40 min. treatment. Even though the maximum IPCE value for the dye is slightly lower than that of the $TiO_2$ layer, it covers a broader wavelength range (from ~400 to 700 nm) in which the standard AM1.5G solar spectrum contains much higher number of photons Np (see Figure A2). The photocurrent $J_{SC}$ can be estimated by integrating (IPCE x Np) over the wavelength range of 400 to 800 nm, which was indeed raised by about 10 times after N719 dye adsorption (see detailed discussions under Figure A2). The above data demonstrates that the photon absorption by $TiO_2$ layer makes only a small contribution to the overall photocurrent of the DSSC cell, but it plays an important role as a barrier layer to prevent electron backflow into the electrolyte so that a high $V_{OC}$ can be maintained. Dye molecule makes the major contribution to the cell performance and determines the magnitude of $J_{SC}$, $V_{OC}$ and IPCE.

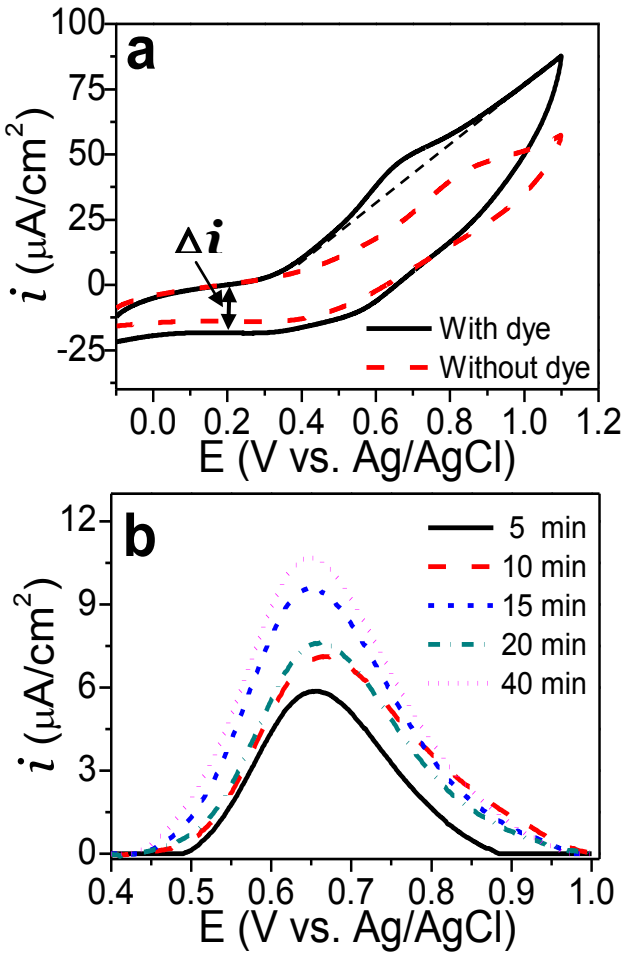


**Figure 2.3. (a) Cyclic voltammogram of a 20 min $TiCl_4$ treated sample with and without dye adsorption. The reference electrode was Ag/AgCl in an acetonitrile filling solution**

**containing 10 mM $AgNO_3$ in 1 M $LiClO_4$. The measurements were taken at 50 mV/s scan rate. (b) Extracted oxidation peaks of adsorbed N719 dye on FTO/glass with different $TiCl_4$ treatment time (5 to 60 min.), derived from the cyclic voltammograms by subtracting the linear background.**

To further characterize the surface properties of the $TiO_2$ barrier layer and its effects on dye molecules adsorption, cyclic voltammetry (CV) measurements were carried out with a series of FTO/glass samples treated with $TiCl_4$ from 5 to 60 min. As shown in Figure 2.3a, a 20 min treated sample shows a tilt CV curve with a high solvent oxidation baseline above ~0.60 V vs. Ag/AgCl (10 mM $AgNO_3$). After adsorption of a monolayer of N719 dye, an oxidation peak is found at ~0.65 V corresponding to oxidation of the N719 dye from Ru(II) to Ru(III). However, it does not show the corresponding reduction wave, indicating that 20 min. treated $TiO_2$ layer serves well as a barrier to block the electron backflow. The Ru(II) oxidation peak can be extracted by subtracting a linear background (thin dashed line in Figure 2.3a) and presented in Figure 2.3b. By dividing the integrated area $A_{CV}$ under the subtracted CV curves with the scan rate $\upsilon$, the total charge Q and subsequently the number of moles of Ru dye molecules $N_{Ru}$ adsorbed at the surface can be derived:

$$Q = \frac{A_{CV}}{\upsilon};\ N_{Ru} = Q/eF \qquad (1)$$

where e is the elementary charge. For 20 min treated sample, the calculated total charge is 4.21 $\times 10^{-7}$ C/cm$^2$, and the adsorbed dye is 4.37 $\times$ $10^{-12}$ mol/cm$^2$. While the $TiCl_4$ treatment time was increased from 5 min. to 60 min., more dye molecules adsorbed onto the electrode surface.

At the meantime, the effective $TiO_2$ electrode surface area $A_{eff}$ can be estimated from the separation in the baseline current of forward and backward scans, which is mostly attributed to the charge-discharge currents to the electrical double layer at the electrode surface. Here the current separation $\Delta i$ was read at 0.20 V and $A_{eff}$ is calculated by:

$$A_{eff} = (\frac{\Delta i}{2})/(C_0 \upsilon) \qquad (2)$$

For anatase $TiO_2$, the specific capacitance is known to be about 90 μF/cm$^2$.[72] By using equation (2), the effective surface area $A_{eff}$ of 20 min treated sample was calculated to be about

22.3 $cm^2$ on each 1.0 $cm^2$ geometric substrate surface area. The trend of the effective $TiO_2$ surface area correlates very well with that of dye adsorption vs. the $TiCl_4$ treatment time.

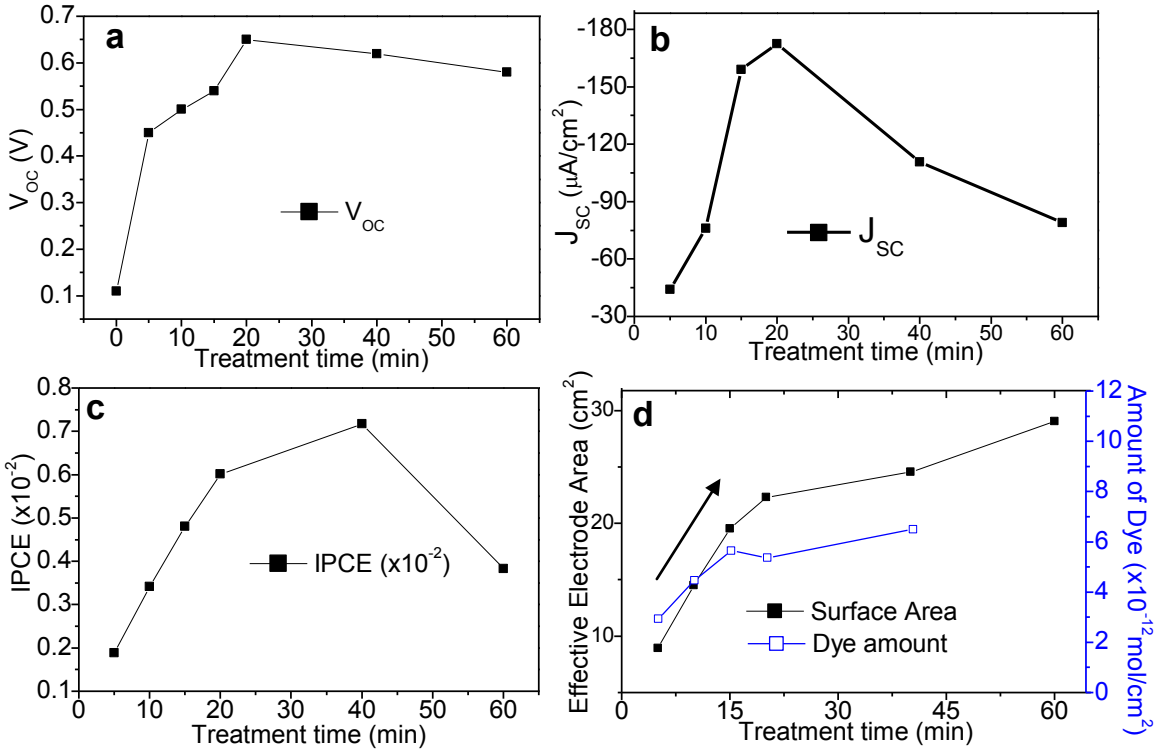


**Figure 2.4. Comparison of (a) $V_{OC}$, (b) $J_{SC}$, (c) the maximum dye IPCE (at 525 nm), (d) Effective surface area $A_{eff}$ on a 1 $cm^2$ geometric surface area and Amount of dye adsorption $N_{Ru}$ vs. the $TiCl_4$ treatment time.**

For comparison, Figure 2.4 shows both of the photovoltaic properties ($J_{SC}$, $V_{OC}$, and the maximum dye IPCE) and electrochemical properties (effective $TiO_2$ surface area $A_{eff}$ and amount of dye adsorption $N_{Ru}$). These data are quite similar to the study on barrier layer in a solid-state DSSC by B.Peng et al[62]. As the treatment time was raised from 0 to 20 min., $A_{eff}$ increased linearly, leading to proportional increase of dye adsorption as shown in Figure 2.4d. This indicates that the $TiCl_4$ treatment builds a porous $TiO_2$ barrier layer in this region and the dye molecules can access and adsorb inside the $TiO_2$ layer instead of only attaching on the outer surface. The treatments longer than 20 min., however, formed plateaus in both of effective surface area and dye adsorption curves, indicating the possibility of transferring the porous $TiO_2$ structure into a more compact film. The $V_{OC}$ curve showed the very similar trend. On the other hand, IPCE and $J_{SC}$ first increased with 0 min. to ~20 min. $TiCl_4$ treatment time, and then

decreased when the time was further increased from ~20 min. to 60 min. It is likely that a thicker compact $TiO_2$ layer may hinder the electron transfer due to the low electrical conductivity.

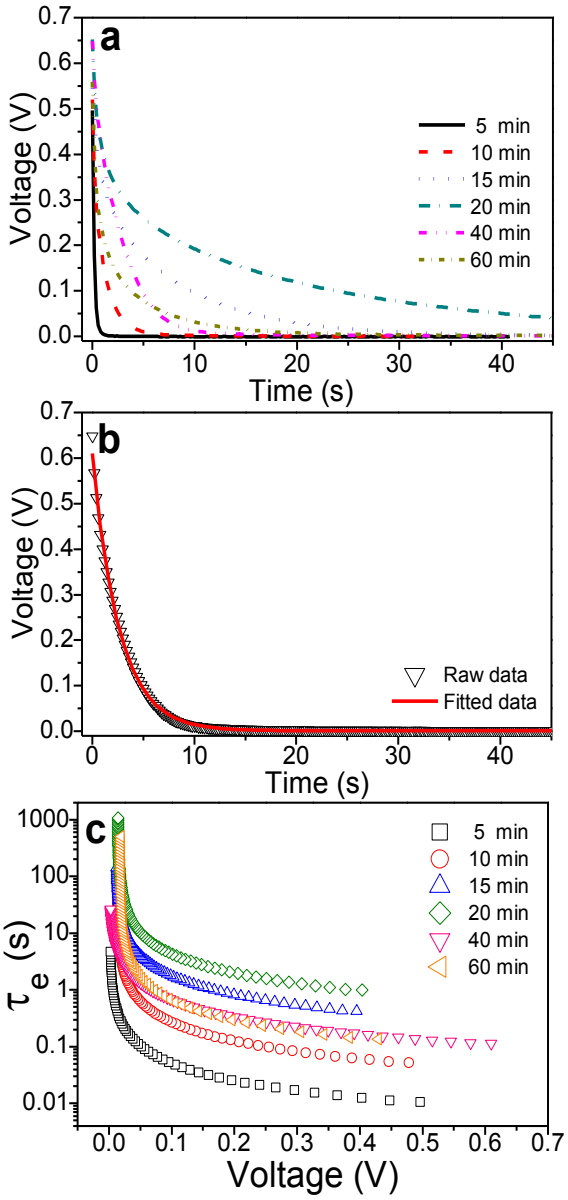


**Figure 2.5. (a) $V_{OC}$ decay curves of the DSSCs made of the photoanodes with different $TiCl_4$ treatment time as light being switched off. (b) Raw data and the exponential fitting of the $V_{OC}$ decay curve of the 20 min. $TiCl_4$ treated FTO/glass photoanode. (c) Comparison of the electron lifetime of different photoanodes.**

Another piece of useful information that can be obtained regarding the barrier layer properties is the lifetime of photoexcited electrons, which can be derived from $V_{OC}$ decay curve after the light is switched off as shown in Figure 2.5. Light was turned on for 20 s to stabilize the $V_{OC}$ and was then turned off while the $V_{OC}$ was measured over time. Apparently the decay rates are strongly dependent on the $TiO_2$ barrier layer as presented in Figure 2.5a. The decay curves can be nicely fitted with the following exponential function (Figure 2.5b):

$$V_{OC} = A + V_{OC}^{0} e^{-(t-t_0)/\tau} \quad (3)$$

The electron lifetime $\tau_e$ can be further derived by:

$$\tau_e = (k_B T/e)(dV_{OC}/dt), \quad (4)$$

where $k_B$ is Boltzmann constant and T is the temperature.[56, 70, 73] The derived $\tau_e$ is a function of $V_{OC}$ as shown in Figure 2.5c. As observed, the 5 min. treated sample had a shortest electron lifetime ranging from about ~0.01 s to ~5 s, while the 20 min. treated sample had a longest lifetime with the whole curve shifted up by nearly two orders of magnitude. More than 20 min. treatment caused the curves to shift down again. The trend agrees very well with the I-V, IPCE, and electrochemical measurements.

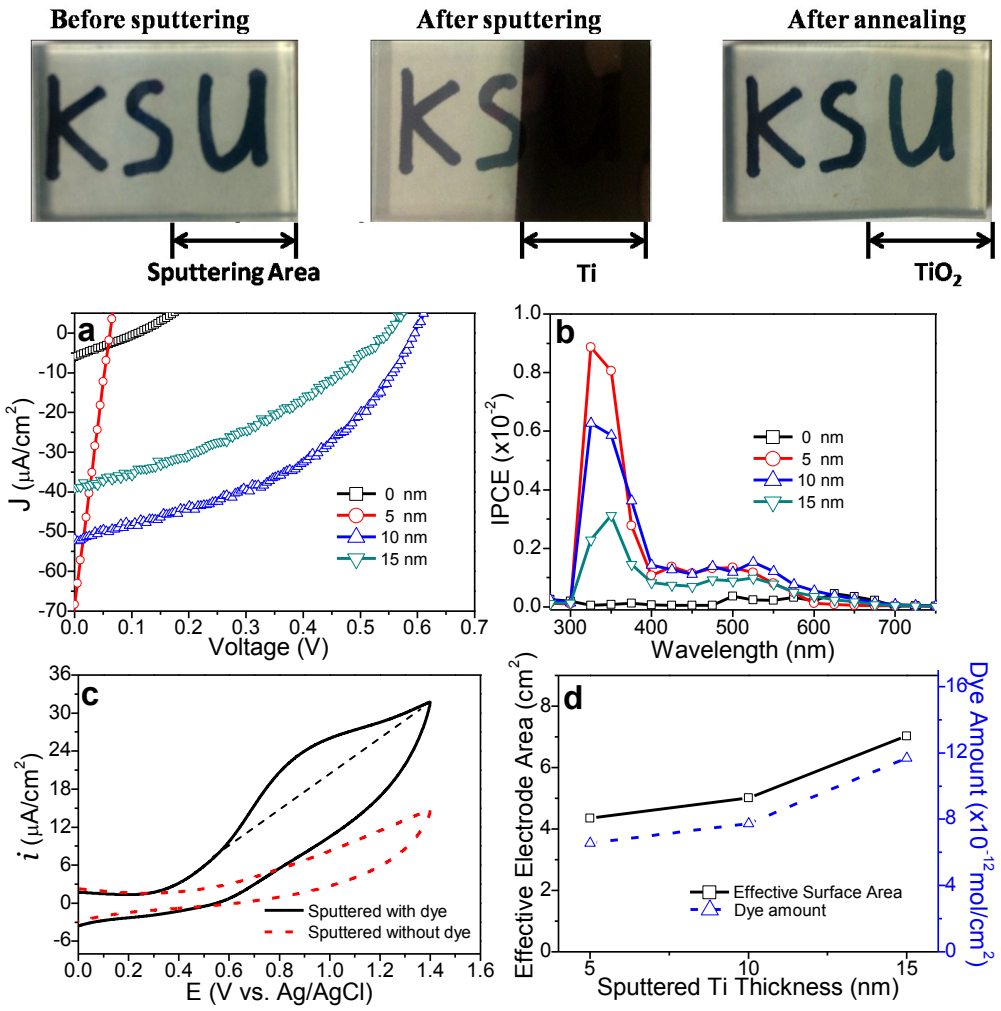


**Figure 2.6. Top Panels: Optical images of a bare FTO/glass sample, this sample after ion-sputtering with 15 nm Ti, and after further thermal annealing in the air at 500 C for 30 min., respectively showing the conversion of opaque Ti into transparent $TiO_2$ film. (a) I-V and (b) IPCE of the DSSCs fabricated with the FTO/glass covered with the sputtering-thermal-annealing produced $TiO_2$ barrier layer started with 5, 10, and 15 nm of Ti metal film. All samples were soaked in the N719 dye solution for dye adsorption. (c) Cyclic voltammograms of a $TiO_2$/FTO/glass sample started with 10 nm sputtered Ti with and without dye adsorption. (d) Comparison of the effective electrode surface area $A_{eff}$ on a 1 $cm^2$ geometric surface area and the amount of dye adsorption $N_{Ru}$ versus the thickness of sputtered Ti.**

Alternately, a compact $TiO_2$ barrier layer can be formed by oxidation of an ion-beam sputtering deposited Ti metal film with thermal annealing in the air at 500 C for 30 min.[65]

Comparing to the non-uniform porous $TiO_2$ layer formed by $TiCl_4$ treatment, this sputtering-thermal-annealing method can produce much more compact and smooth $TiO_2$ barrier layers. The starting Ti film thickness can be precisely controlled (down to 0.1 nm) with the High-Resolution Ion Beam Coater. The top panels in Figure 2.6 show the conversion of an opaque Ti film into a transparent $TiO_2$ film by the thermal annealing process. Both I-V curves (Figure 2.6a) and IPCE curves (Figure 2.6b) of the DSSCs made of N719-sensitized $TiO_2$/FTO/glass anodes showed strong dependence on the sputtered Ti thicknesses (5, 10, and 15 nm). Though the 5 nm sputtered sample gave the largest $J_{SC}$, the $V_{OC}$ of some DSSCs was very low, likely due to the incomplete $TiO_2$ coverage or open grain boundaries at this small thickness. Thicker $TiO_2$ barrier layer gave much larger and reliable $V_{OC}$ and decent I-V curves showing high fill factors. The 10 nm sputtered sample gave the best overall photovoltaic properties. Further increase of sputtered Ti to 15 nm turned to lower both $J_{SC}$ and $V_{OC}$. The I-V and IPCE of the DSSCs without dye adsorption (Figure A4) showed similar trend. The sputtering-thermal-annealing $TiO_2$ barrier layer somehow affected electron transfer more than that by $TiCl_4$ treatment. In addition, comparing to that of $TiCl_4$ treated sample, the IPCE value of dye molecules at ~525 nm is much lower eventhough that of $TiO_2$ (at ~350 nm) are comparable. The dye to $TiO_2$ ratio in the sputtering-thermal-annealing samples was generally much lower than that in $TiCl_4$ treated samples. It is possible that the sputtering-thermal-annealing $TiO_2$ barrier layer was too compact so that the dye molecules only adsorbed on the outer surface. This hypothesis was confirmed by the CV measurements shown in Figures 2.6c and 2.6d. Using the same method discussed earlier, the effective $TiO_2$ surface area $A_{eff}$ and the total amount of dye adsorption $N_{Ru}$ can be derived from the CV curves. As shown in Figure 2.6d, both of these quantities only slightly increased as the thickness of the $TiO_2$ barrier layer was raised (by increasing sputtered Ti thickness). The small change can be attributed to the small increase in outer surface roughness in thicker $TiO_2$ layers.

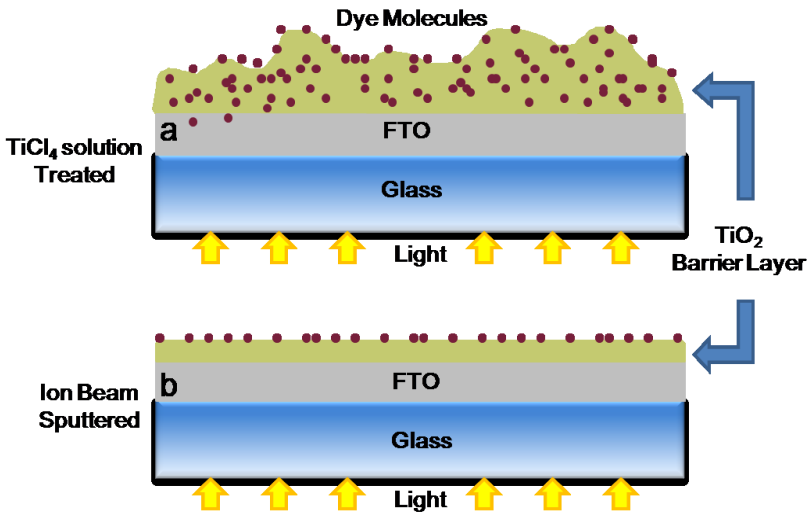


**Scheme 3. Schematic illustration of the differences of the $TiO_2$ barrier layers formed by (a) $TiCl_4$ treatment and (b) Ti sputtering followed by thermal annealing.**

The structural differences of the $TiO_2$ barrier layers formed by $TiCl_4$ treatment and sputtering-annealing of Ti are summarized in Scheme 1. Ideally, the conformal compact barrier layer by sputtering-annealing of Ti metal would simplify the structure and thus may be a better choice. However, the chemical and materials properties of the $TiO_2$ film by $TiCl_4$ treatment were better for DSSCs. Particularly, 20 min $TiCl_4$ treated FTO/glass appeared to be the best $TiO_2$ barrier layer with ideal porosity, compactness, good electron transport, and effective backflow blocking effects. Longer $TiCl_4$ treatment tended to degrade the performance. The materials difference is further illustrated by the Raman spectra in Figure A5, which confirmed that only the $TiCl_4$ treatment produced the desired anatase $TiO_2$ crystal structure. A sharp peak at the Raman shift of ~143 $cm^{-1}$ was observed in all $TiCl_4$ treated samples with the peak intensity increasing quickly with the treatment time. In contrast, only a small anatase shoulder at ~143 $cm^{-1}$ as well as those of rutile crystal at 448 and 610 $cm^{-1}$ were barely observed in the samples by sputtering-annealing of Ti metal. It may form amorphous or rutile crystallites during thermal oxidation of the Ti metal at 500° C as reported by Zhu et al.[74] This partially explains why the performance of DSSCs made with the sputtering-annealing method was worse than those by $TiCl_4$ treatments since anatase $TiO_2$ is known a better crystalline phase for DSSCs[75].

## Conclusions

In summary, we have demonstrated two methods, the wet chemical treatment of FTO electrode with an aqueous $TiCl_4$ solution and thermal oxidation of sputter-coated Ti metal film,

in preparing thin $TiO_2$ films as the barrier layer to prevent the photoelectron backflow from TCO to electrolyte or recombining with the holes at the TCO surface during DSSC operation. The structural and materials properties of the $TiO_2$ barrier layer were systematically characterized with electron microscopy, Raman spectroscopy, I-V and IPCE measurements under light illumination, and cyclic voltammetry. The characterization results showed consistent effects of the thickness and structure of the $TiO_2$ barrier layer on the DSSC performance. The method by $TiCl_4$ solution treatment produced a non-uniform porous $TiO_2$ film whose interior surface was accessible by the N719 dye while the method by sputtering-annealing of Ti metal formed a smooth compact $TiO_2$ film with N719 dye only adsorbed on the outer surface. Overall, the DSSCs fabricated with photoanodes by 20 min. $TiCl_4$ treatment showed the best performance, likely due to the formation of desired anatase crystallites at the optimum thickness. Such thin-film DSSCs may be used as a model system to test the photovoltaic effects of new dyes or macromolecular sensitizers which cannot easily access the interior pores of traditional DSSCs.

# Chapter 3 - VACNFs as a New Type of Counter Electrode in DSSCs

## Abstract

A new type of counter electrode in dye-sensitized solar cell (DSSC) system using the vertically-aligned carbon nanofibers (VACNFs) structure was demonstrated. VACNF counter electrode was fabricated on a Si substrate using plasma enhanced chemical vapor deposition (PECVD). The structural properties of VACNFs were studied by scanning electron microscopy, transmission electron microscopy and Raman spectroscopy. Cyclic voltammetry characterization showed that the VACNF electrode had a large specific surface area of 125 $cm^2$ over 1 $cm^2$ window. I-V measurement demonstrated that the DSSCs made of a VACNF counter electrode had a comparable efficiency of 4.98% to that of DSSC with a Platinum (Pt) counter electrode, which had an efficiency of 5.1%. Electrochemical impedance spectroscopy results showed that the charge transfer resistance of VACNF electrode was smaller than Pt electrode, and VACNF electrode had a lower series resistance due to good electronic conductivity. Overall, VACNF counter electrode showed a comparable performance to Pt counter electrode but potentially at lower cost and sustainable materials.

## Introduction

Dye-Sensitized Solar Cells (DSSCs) have drawn great attentions for their good efficiency and low cost in recent decades. Counter electrode is a very important component in the DSSC system, it collects electrons from outer circuit and reduces $I_3^-$ into $I^-$ in the electrolyte. Currently the most widely used material for counter electrode is Pt, which has good catalytic activity for the reduction of the $I_3^-$ mediator. Its high cost and limit supply, however, is one of the main problems that prevent people from using it for large-scale solar energy applications. Development of a new alternative counter electrode material is urgent.

Carbon has emerged as a new promising counter electrode material for replacement of Pt. It has benefits of low cost, good stability, good catalytic activity, good electronic conductivity, easy fabrication and very large surface area. So far a number of forms of carbon have been reported as materials for counter electrodes, such as multi-walled carbon nanotubes

(MWCNTs)[34, 76-79], single-walled carbon nanotubes (SWCNTs)[37, 80-83], carbon nanofibers (CNFs) [84-86],and graphene [87-92].

In this study, a new 3-D vertically-aligned carbon nanofiber (VACNF) structure is introduced to be a replacement for Pt. VACNFs are fabricated by Plasma-Enhanced Chemical Vapor Deposition (PECVD) method. The 3-D VACNF structure provides an extremely large counter electrode surface area of 125 $cm^2$ over 1 $cm^2$ testing area. The large surface area ensures a good contact between counter electrode and electrolyte, which leads to a better and more stable catalytic activity between VACNFs and redox couple in the electrolyte. The DSSC built with VACNFs counter electrode showed a good conversion efficiency of 4.98%, which is comparable to the 5.1 % efficiency of DSSCs using our homemade Pt counter electrodes.

## Experimental

**Preparation of Photoanode of DSSC.** Commercial fluorine-doped tin oxide (FTO) glass (Pilkington Glass, Lathrop, CA) was used as the photoanode substrate, which was first cleaned by sonication in isoproponal, ethanol and acetone each for 15 min. In the second step, FTO anodes were treated with 40 mM $TiCl_4$ solution, at 70℃ in oil bath for 20 min, which was reported as an optimal treatment time to create a $TiO_2$ barrier layer in the previous paper by our group. The photoanode was annealed in the tube furnace in open air at 500℃ for 30 min to form a anatase $TiO_2$ barrier layer. Third, the photoanode with barrier layer was then pasted with $TiO_2$ nanoparticles (Solaronix, Aubonne, Switzerland) using doctor blade method and the pasted photoanode was annealed again in open air at 500℃ for 30 min to form anatase $TiO_2$ nanoparticle layer. Finally, the annealed anode was immersed in a 0.5 mM *cis*-diisothiocyanato-bis (2,2'-bipyridyl-4,4'-dicarboxylato) ruthenium (II) bis (tetrabutylammonium) (N-719 dye) in dried ethanol solution (Solaronix, Aubonne, Switzerland) for 12 h for dye adsorption. The samples were rinsed with dry ethanol to remove physisorbed dyes.

**Preparation of Cathode of DSSC.** Two 1 mm holes were drilled at the diagonal corners of the 1$cm^2$ window of the commercial Si wafer (WaferNet. Inc, San Jose, California) for VACNF electrode and FTO-coated glass for Pt electrode. A 100 nm thick layer of Cr and 22.5 nm Ni was then sputtered onto the Si wafer using high-resolution ion beam coater (Model No. 681, Gatan

Inc., Pleasanton, CA). The sputtered substrate was then put into the PECVD system (Aixtron, Cambridge, United Kingdom) to grow the vertically-aligned carbon nanofibers, then the as grown VACNF electrode was soaked into $HNO_3$ to remove the amorphous carbon to expose the active graphitic edges. The FTO-glass was sputtered with 25 nm thick Pt using the above ion beam coater. The Pt sputtered electrode was annealed at 450℃ in the air for activation.

**Assembly and Characterization of DSSCs**. The anode and counter electrode were bonded through a 60 μm thick hot melt spacer (Solaronix, Aubonne, Switzerland) following our previous procedure.[66] Then the Iodolyte AN-50 electrolyte (Solaronix, Aubonne, Switzerland) consisting of 50 mM triiodide, 0.1 M LiI, and 0.5 M 1,2-dimethyl-3-propylimidazolium iodide in acetonitrile was filled in the cell by a syringe. The assembled cell with an active area of 1 cm × 1 cm was characterized under one sun illumination with a 300 W Xe lamp solar simulator and an AM 1.5G filter (Newport, Irvine, CA) to obtain the photocurrent-voltage (I-V) curve.

**Electrochemical and Materials Characterization**. Cyclic voltammetry was carried out with a potentiostat (CHI 440A, CH Instruments, Austin, TX) in the Iodolyte AN-50 electrolyte mentioned above using a three-electrode setup vs. a Pt counter electrode and a Ag/AgCl reference electrode (filled with acetonitrile solution containing 10 mM $AgNO_3$ in 1 M $LiClO_4$) to characterize the catalytic activity. Scanning electron microscopy (SEM) was carried with a field-emission system (FEI Nano430). Transmission electron microscopy (TEM) was measured. Raman spectra were measured with a DXR Raman microscope (Thermo Electron, WI) using 50X objective, 530 nm laser, and 5 mW laser power. Electrochemical impedance spectroscopy was carried out with an electrochemical workstation (Parstat 2273, Princeton Applied Research, Oak Ridge, TN) under one sum illumination.

## Results and Discussion

VACNFs grown by PECVD have cylindrical outer structure with diameters ranging from a number of nanometers to several hundreds of nanometers and lengths varying from microns to hundreds of microns. The internal structure with different arrangement of graphene layers is what makes VACNFs different from CNTs and conventional carbon nanofibers. Figure 3.1b shows the structure of VACNFs, and different internal structures can be formed based on a

different cone angle α. With cone angle α = 0, it gives a bamboo-like structure [93, 94], which results in a smooth outer wall for each CNF, and this type of CNF is known as carbon nanotubes (CNTs). The other type is just as what is shown in Figure 3.1b with a cone angle α > 0, which forms an internal structure consists of cone-like stacked graphene layers with a defect rich outer wall. This cone structured VACNFs is the type that was used in this study.

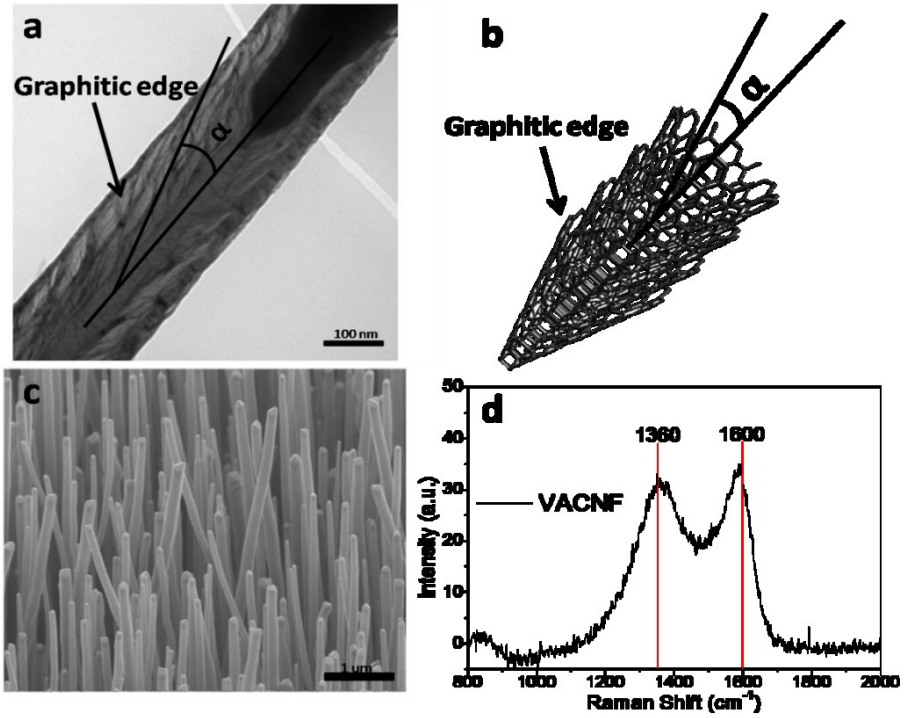


**Figure 3.1. (a) TEM image of a single VACNF with cone like inner structure shown, (b) Schematic drawing of a single VACNF with same structure shown in (a), (c) SEM image at 45□ perspective view of VACNFs, (d) Raman characterization of VACNF.**

Layers of cone-structured graphene were stacked, forming a stacked cone-like or fishbone-like structure. Due to stacked graphene layers, the graphitic edges of each graphene layer were exposed and act as the outer wall of VACNFs. With the active graphitic edges, the catalytic activity rate with the $I^-/I_3^-$ redox couple in electrolyte will be improved. Figure 3.1a and 3.1c are the TEM and SEM images of the as grown VACNFs. The cone-like structure is clearly demonstrated in the TEM image. Good uniformity and high density of about $5.6\times10^9$ VACNFs per 1 $cm^2$ grown on Si substrate is shown in then SEM image. With such a high VACNF density, the specific surface area of a VACNF electrode over 1 $cm^2$ window can be approximately

calculated using the dimension of a single VACNF, which has a surface of about $2.4\times10^{-8}$ $cm^2$. The specific surface area calculated was 125 $cm^2$ over the 1$cm^2$ window, respectively. With such high specific surface area, the catalytic activities between VACNF electrode and electrolyte can be further improved. Raman characterization is shown in Figure 3.1d. Peak around 1600 cm-1 (G-band) demonstrates the formation of graphene structure, and the peak around 1360 cm-1 (D-band) demonstrates the defects in the VACNFs, which is mostly due to the exposed graphitic edges.

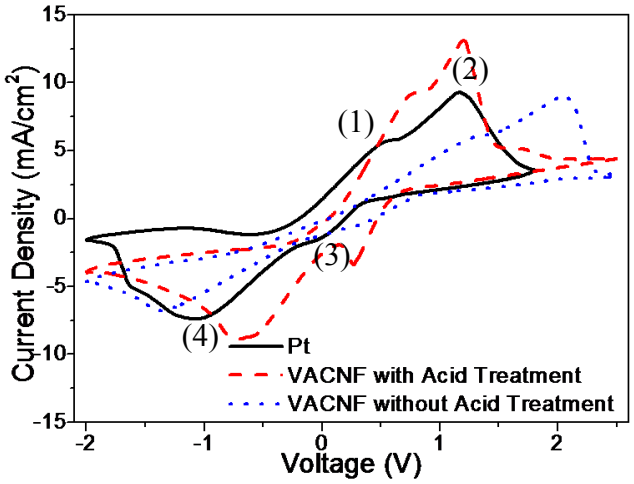


**Table 1. Peak separations of each sample**

| | $Ep_1$-$Ep_4$ (V) | $Ep_2$-$Ep_3$ (V) |
|---|---|---|
| Pt | 1.68 | 1.11 |
| VACNF Untreated) | 1.56 | 0.95 |
| VACNF (Treated) | 2.86 | 1.78 |

**Figure 3.2, Cyclic voltammogram of counter electrodes using different materials. Solid line stands for electrode with Pt, dashed line stands for electrode using VACNFs after acid treatment, and dotted line stands for electrode using VACNF before acid treatment.**

Cyclic Voltammetry is a very useful and important technique to study the electrochemical properties of VACNFs. Figure 3.2 shows the CV curves of different types of counter electrodes. Two oxidation and two reduction peaks were observed due to the following two redox reactions (1), (2), (3) and (4).[84, 95, 96]

$$2I^- \rightarrow I_2^- + e^- \quad (1)$$

$$I_2^- + I^- \rightarrow I_3^- + e^- \quad (2)$$

$$I_3^- + e^- \rightarrow I_2^- + I^- \quad (3)$$

$$I_2^- + e^- \rightarrow 2I^- \quad (4)$$

Equation (1) and (2) explain that in the DSSC system, electrons are injected into the

oxidized dye molecules from electrolyte to regenerate them, and the reduction reaction of produced $I_3^-$ ions on the counter electrode is shown in equations (3) and (4). Dotted CV curve in Figure 3.2 represents the VACNFs without acid treatment, which means the amorphous carbon around the VACNFs was not removed. Compared to CV curve of the Pt electrode, the VACNFs electrode without acid treatment had a lower current density and a broader peak separation, which demonstrates that the untreated VACNF electrode has a slower reaction rate than Pt electrode. Dashed CV curve of VACNF with acid treatment in Figure 3.2 shows a larger current density and a smaller peak separation than both the Pt electrode and the VACNF electrode without acid treatment, which demonstrates a faster electron transfer rate that is due to the exposed graphitic edges[96-98] after acid treatment, which removed the amorphous carbon deposited around the VACNFs. Higher electron transfer rate also means a higher reaction rate of the two reactions mentioned above, which can further improve the DSSC performance, and all these are attributed to the large specific surface area and large amount of exposed graphitic edges in the VACNF counter electrode.

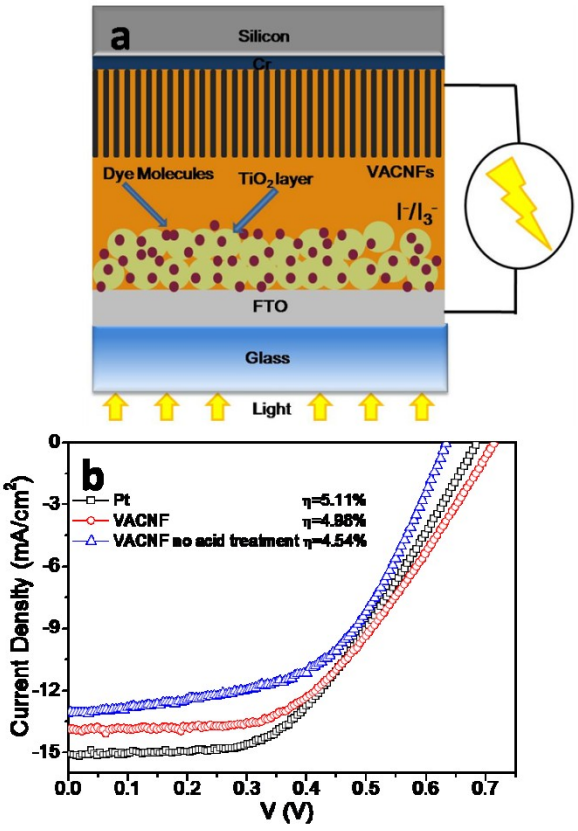

**Figure 3.3. (a) Schematic drawing of the structure of DSSCs with VACNFs as the counter electrode, (b) IV curve comparison between DSSCs using Pt counter electrode, acid-treated VACNF counter electrode, and untreated VACNF counter electrode without acid treatment.**

Schematic of the structure of DSSC using VACNF counter electrode is shown in Figure 3.3a, the traditional Pt counter electrode has been replaced with VACNF electrode, which has larger specific surface area with large number of exposed graphitic edges that help reactions with electrolyte. I-V measurement is shown in Figure 3.3b. The cell with Pt counter electrode had a higher $J_{SC}$ of 15.12 mA/cm$^2$ and a $V_{OC}$ of 0.689 V. The cell with VACNF counter electrode had a $J_{SC}$ of 13.8 mA/cm$^2$ and a $V_{OC}$ of 0.713 V, respectively. The cell with VACNF electrode without acid treatment had a $J_{SC}$ of 13.1 mA/cm$^2$ and a $V_{OC}$ of 0.634 V, which shows the importance to improve the catalytic activities by removing amorphous carbon with acid treatment. The $V_{OC}$ value is consistent with the reduction potential shift shown in Figure 3.2. Overall, the efficiency for cell with VACNF counter electrode without acid treatment was 4.54%, and VACNF cell with acid treatment was 4.98%, which is comparable to 5.1% of the cell with Pt counter electrode.

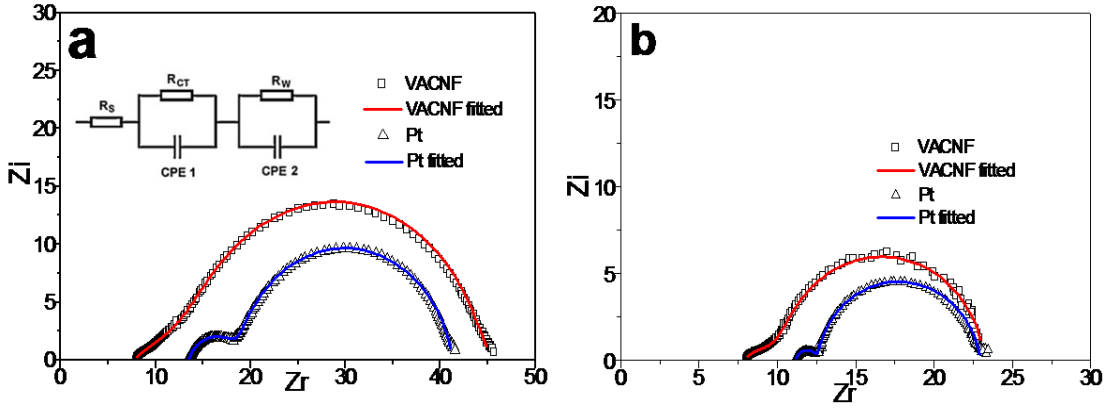


**Figure 3.4. EIS plot of DSSC using a Pt counter electrode and DSSC using an acid-treated VACNF counter electrode under dark (a) and illumination (b).**

In order to further investigate the electrochemical properties and electron transfer in DSSC system, EIS was carried to measure both cells with VACNF electrode and Pt electrode. Figure 3.4 shows the EIS spectra of cells with VACNF electrode (in square and the fitted data shown in red line) and Pt electrode (in triangle and fitted data shown in blue line). The equivalent circuit is shown in inset of panel a. A small semi-circle at high frequency region (200 Hz to 100 kHz) and

a large semi-circle at middle frequency region (200 Hz to 0.1 Hz) were observed in Pt electrode; however the small semi-circle can barely be seen in VACNF electrode. The first (small) semi-circle at high frequency region is related to the interfacial capacitance (CPE1) and charge transfer resistance ($R_{CT}$) at the interface of counter electrode/electrolyte. The second (large) one at middle frequency region is related to the interfacial capacitance (CPE2) and charge transfer resistance ($R_W$) at the interface of dye/$TiO_2$/electrolyte[90, 99]. It can be observed that the $R_{CT}$ values of cell with VACNF counter electrode at both dark ($R_{CT}$ = 1.217 ohm) and illumination ($R_{CT}$ = 0.787 ohm) conditions are smaller the ones with Pt counter electrode ($R_{CT}$ =5.35 ohm under darkness, and $R_{CT}$ = 1.37 under illumination), which demonstrates that the large specific surface area and large numbers of active graphitic edges help to improve the reaction and charge transfer rate between the interface of counter electrode and electrolyte. The series resistance ($R_S$) of VACNF electrode is lower than Pt electrode due to higher electronic conductivity, which demonstrates the VACNFs as effective electrodes. .

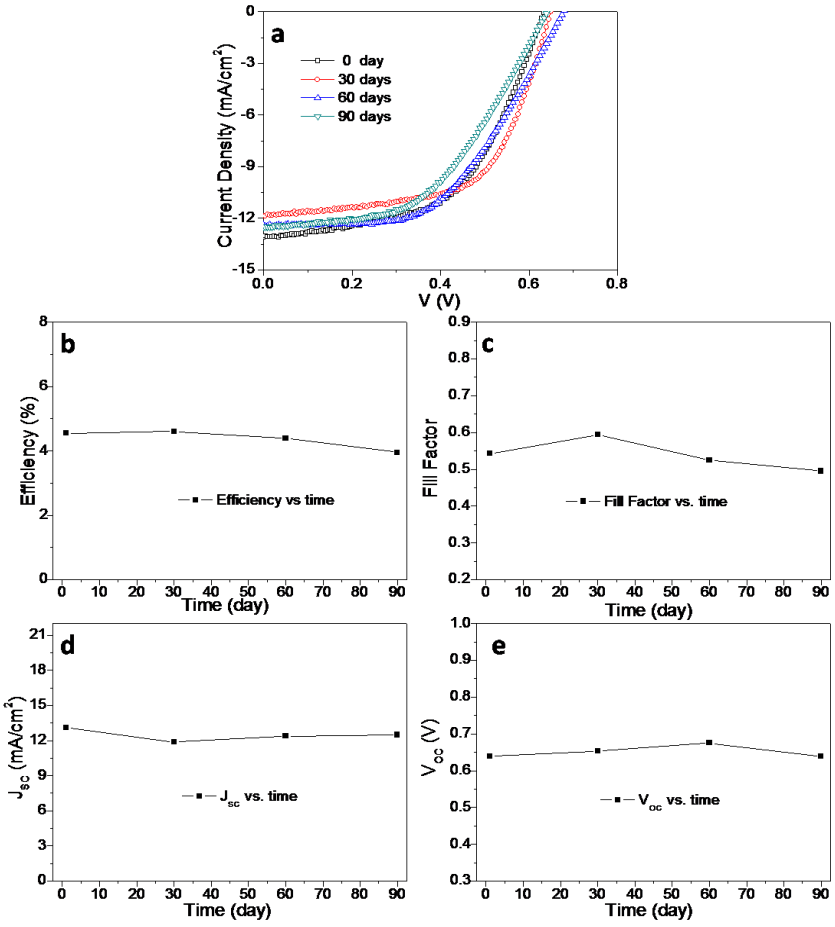

**Figure 3.5. Stability measurement of a DSSC with a VACNF counter electrode over 90 days, (a) I-V curves vs. time, (b) efficiency vs. time, (c) fill factor vs. time, (d) $J_{SC}$ vs. time, (e) $V_{OC}$ vs. time.**

I-V measurement of a similar DSSC with non-acid-treated VACNF counter electrode was carried out every 30 days to show the good stability of using this new type of VACNF counter electrode. There were some small fluctuations of each parameter, and the overall efficiency after 90 days was decreased by only 13% from 4.54% on the first day to 3.95% on the 90$^{th}$ day. The good stability was attributed to the good electrical and chemical stability of VACNFs.

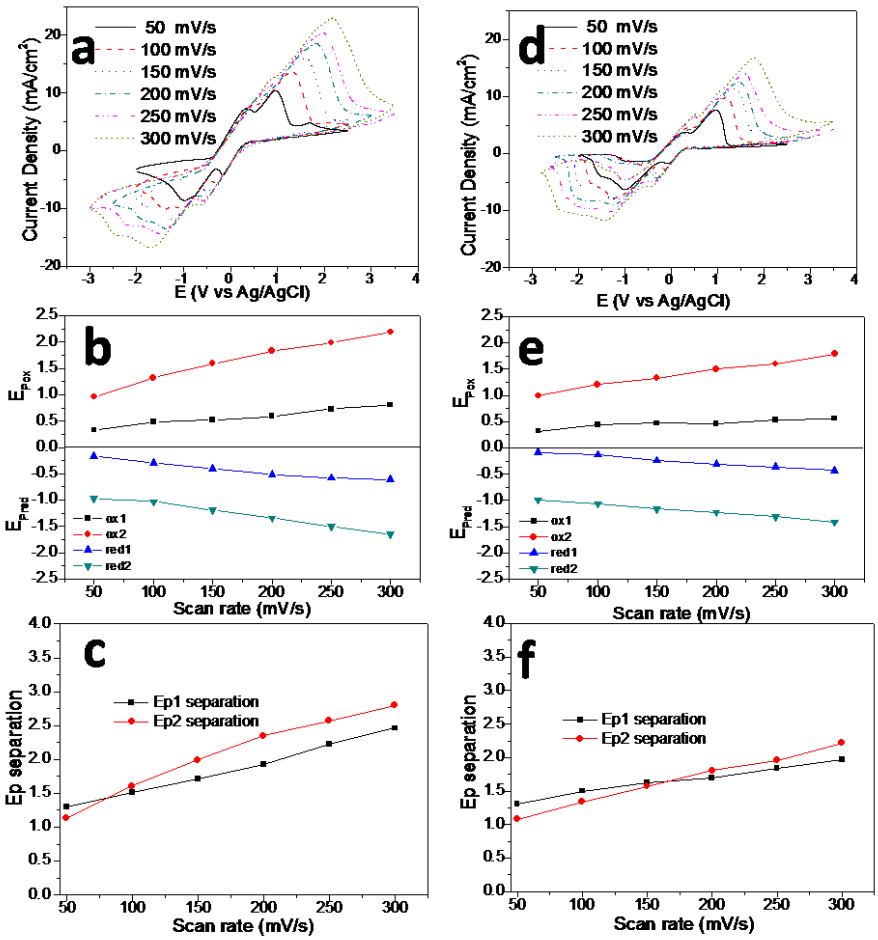


**Figure 3.6. Cyclic voltammetry measurement of: (a) VACNF counter electrode and (d) Pt counter electrode with different scan rates. Oxidation and reduction peak potential vs. scan rate and peak separation vs. scan rate of both electrode (b, c for VACNF counter electrode and e, f for Pt counter electrode).**

In order to further compare VACNF electrode with Pt electrode, cyclic voltammetry measurement was carried out with different scan rates, and the oxidation and reduction peak potential and peak separation of both electrodes were measured and compared with the scan rate varying from 50 mV/s to 300 mV/s. VACNF electrode was very comparable with Pt electrode as demonstrated in Figure 3.6. As the scan rate increased, the peak separation increased slightly as what was shown from Pt electrode. This demonstrated that the redox reactions are quasi-reversible but comparable with both electrodes. The reaction rates are not very fast but sufficient to match the photocurrent as in traditional DSSCs.

## Conclusions

In summary, a 3-D VACNF counter electrode was fabricated by PECVD. The structural and materials properties of VACNFs were characterized with TEM, SEM and Raman spectroscopy. I-V measurement, cyclic voltammetry, and EIS were carried out to study the cell performance and electrochemical properties. The characterization results showed that the VACNF structure had a large specific surface area of 125 $cm^2$ over 1 $cm^2$ window with a big number of active graphitic edges that improve the catalytic activity between counter electrode and electrolyte. Comparable cell efficiency (4.98%) was demonstrated compared to the DSSC with Pt counter electrode (5.1%), and good cell stability over 90 days was shown. Overall, the VACNF counter electrode can be served as a good alternative to the Pt electrode with a comparable performance and lower cost.

# Chapter 4 - $TiO_2$ Coated VACNFs

## Abstract

$TiO_2$ nanoparticle coated vertically-aligned carbon nanofiber (VACNF) was fabricated by the metal-organic chemical vapor deposition (MOCVD) of a $TiO_2$ layer onto VACNFs. Various deposition time and deposition partial pressure were tested. As the deposition time increased from 30 min to 120 min, it changed from no coating into a uniform and tightly packed $TiO_2$ nanoparticle coating around the VACNFs (shown in SEM images) with a coating thickness of ~ 50 nm (shown in TEM images). Such core-shell-$TiO_2$ VACNF structure can be used to build the photoanode in dye-sensitized solar cells (DSSCs). The core-shell structure can help prevent the electron recombination and back flow in the DSSC system just like what a $TiO_2$ barrier layer does as reported. With the VACNF core, electron transfer and specific surface area can be further improved.

## Introduction

Studies about dye sensitized solar cell have been carried out in the recent decades. The traditional structure of a DSSC uses $TiO_2$ nanoparticles to attach dye molecules that absorb light. One disadvantage of this structure is the severe electron recombination and the respectively slow electron transfer rate through the semiconducting $TiO_2$ nanoparticle network. Works about using other structures to replace the mesoporous $TiO_2$ nanoparticle network have been reported as using $TiO_2$ nanotubes [26, 27, 100], ZnO nanotubes and nanowires[101, 102,103-105], mixture of $TiO_2$ nanoparticles and graphene [106], and mixture of $TiO_2$ nanoparticles and carbon nanotubes[107]. By using the direct electron pathways or mixing with conductive materials, a faster electron transport can be achieved. This work represents a new photoanode structure based on the $TiO_2$ nanoparticle coated vertically aligned carbon nanofibers (VACNFs) using metal organic chemical vapor deposition (MOCVD) process. VACNFs were fabricated using plasma enhanced chemical vapor deposition (PECVD) on the three different solid substrates. The as grown VACNFs, with large amount of active graphitic edges and a big specific surface area, can obtain a well packed and uniform $TiO_2$ coating around each single VACNF and provide a large electrode surface area. $TiO_2$ coating was deposited using MOCVD process. The deposition

condition was studied using various deposition time (30 min to 120 min) and different partial pressure (150 mTorr, 300 mTorr and 600 mTorr). SEM and TEM images were taken to examine the deposition of each sample, and the optimal condition was found to be 300 mTorr with 120 min deposition time.

Three substrates are FTO coated quartz, Cu and Si. FTO coated quartz substrate was used in the study of DSSC due to its transparency. Si substrate was used mainly for the MOCVD condition study and Cu substrate can be used in other application, such as Lithium ion battery study. The $TiO_2$ coated VACNFs grown on FTO coated quartz was used as a new architecture for the DSSC system. With the VACNF core, electron can transfer much faster than the traditional $TiO_2$ nanoparticle network. The $TiO_2$ nanoparticle coating around the VACNF can act as a barrier layer to minimize the electron recombination and back flow between the interface of dye molecule and VACNFs, the interface of electrolyte and VACNFs, and the interface of dye molecule and FTO coated quartz electrode. With the high electrode surface area and fast electron transfer rate, this new photoanode structure can be used in the future DSSC study to obtain a more efficient DSSC.

## Experimental

**Fabrication of VACNFs.** Commercial Si wafer was used as substrate for VACNF growth, which was first cleaned by sonication in isoproponal, ethanol and acetone each for 15 min. In the second step, Si wafer was dried in oven and put into high-resolution ion beam coater (Model No. 681, Gatan Inc., Pleasanton, CA). 100 nm thick layer of Cr and 22.5 nm Ni was then sputtered onto the Si wafer. The sputtered substrate was then put into plasma-enhanced chemical vapor deposition (PECVD) system to grow the VACNFs at 750℃. Copper foil was used as the substrate to grow VACNFs for battery testing. The commercial Cu foil was sputtered with 100 nm Cr and 22.5 nm Ni using the same ion beam coater mentioned above, and was then put into PECVD system to grow VACNFs at 750℃. FTO coated quartz substrate (Solaronix, Aubonne, Switzerland) was used as substrate for DSSC testing. Substrate was cleaned following the same procedures as Si wafer, dried and put into ion beam coater. 22.5 nm Ni was sputtered onto the FTO coated quartz substrate, and the substrate was moved into PECVD for VACNF growth at 550℃.

**MOCVD process for coating $TiO_2$ on VACNFs**. $TiO_2$ was coated onto different substrates using MOCVD process at 500℃ under a partial pressure of 300 mTorr with a bass pressure of 70 mTorr for 3 hrs.

**Electrochemical and Materials Characterization**. Cyclic voltammetry was carried out with a potentiostat (CHI 440A, CH Instruments, Austin, TX) in an acetonitrile solution containing 0.1 M $LiClO_4$ using a three-electrode setup vs. a Pt counter electrode and a Ag/AgCl reference electrode (filled with acetonitrile solution containing 10 mM $AgNO_3$ in 1 M $LiClO_4$) to characterize the N719 dye adsorption and electrochemical activity. Scanning electron microscopy (SEM) was carried with a field-emission system (FEI Nano430). Transmission electron microscopy (TEM) was measured.

## Results and Discussion

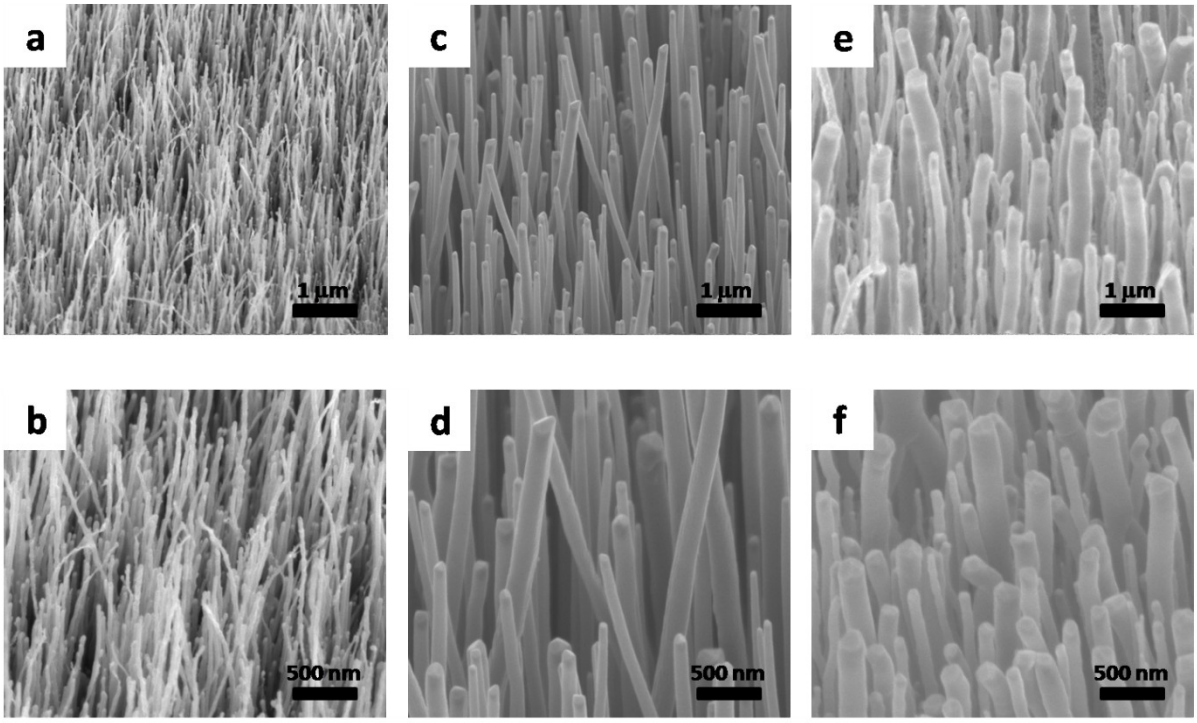


**Figure 4.1. 45°perspective view of SEM images of VACNFs grown on (a, b) FTO coated quartz substrate with a diameter about 40 nm, (c, d) Cu substrate with a diameter about 100 nm, (e, f) Si substrate with a diameter of 100 nm.**

A good substrate is the base for a good sample. Figure 4.1 shows the SEM images of 3 different substrates on where the VACNFs were grown. Figure 4.1a and 4.1b are the images of VACNFs grown on the FTO coated quartz substrate using PECVD. 750°C was used as the growth temperature as the other two substrates. However, under that high temperature, the FTO coating will degrade, which leads to a bad VACNF growth. The FTO degradation temperature is around 550 – 600°C, so 550°C was then set as the growth temperature. Surprisingly, the result turned out with quite good uniformity, and it was reproducible. 750°C was used for the other two substrates and good quality and uniformity were obtained. Compare the VACNFs in Figure 4.1a and 4.1b to the other images, smaller diameter of the VACNFs was observed, and it may be due to the low growth temperature, which resulted in a smaller diameter. All the substrates were later coated with $TiO_2$ nanoparticles using MOCVD method. The one with FTO coated quartz substrate was used as the photoanode in a DSSC system because the FTO coated quartz is transparent. The one with Cu substrate was later used as the part in the Lithium ion battery study. The one with Si substrate is most reliable and was used mainly to characterize the MOCVD coating condition.

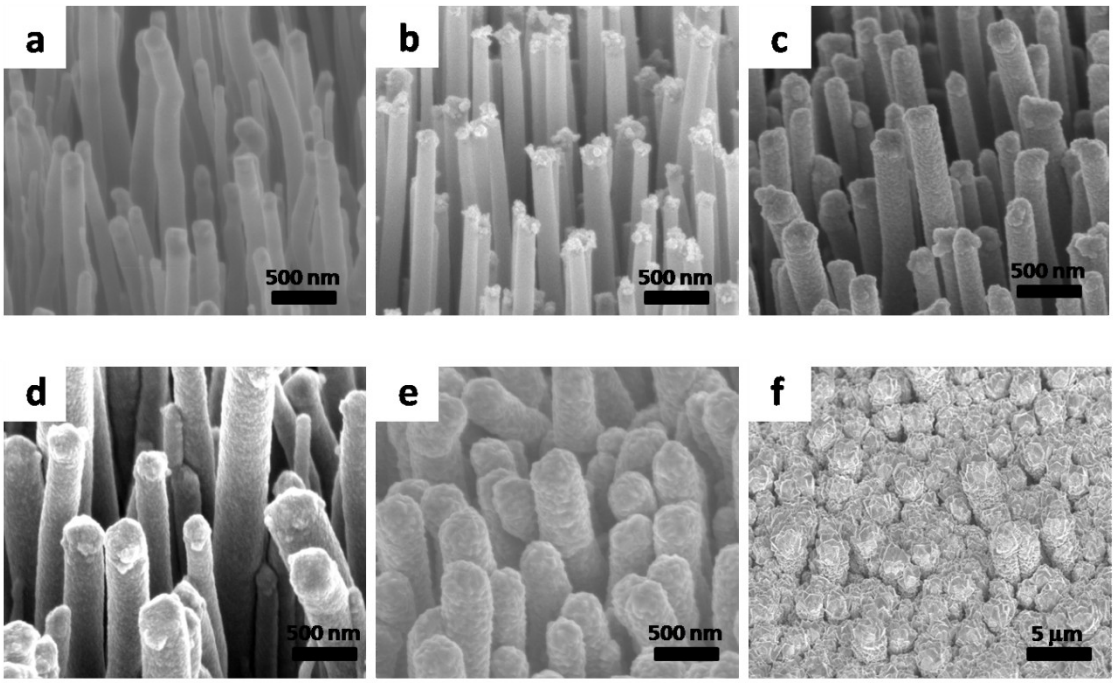


**Figure 4.2. 45°perspective view of SEM images of $TiO_2$ coating using MOCVD process on the as-grown VACNFs on Si with various growth time and partial pressure (a) 150 mTorr**

**for 30 min, (b) 300 mTorr for 30 min, (c) 300 mTorr for 60 min, (d) 300 mTorr for 90 min, (e) 300 mTorr for 120 min, (f) 600 mTorr for 60 min.**

Figure 4.2 demonstrates different $TiO_2$ MOCVD coating results with different temperature and partial pressure. The coating condition in Figure 4.2a was 150 mTorr as the partial and 30 min as coating time, which was obtained from a previous study from our group[108]. However, no coating was observed. The MOCVD used in this study was totally rebuilt to better control the deposition condition. It now has a better vacuum level that 70 mTorr can be obtained as the base pressure. A small change in the MOCVD condition can cause a huge difference in deposition results. Thus the parameters were systematically investigated. Figure 4.2b shows the coating result of 300 mTorr with 30 min coating time. Some small amount of $TiO_2$ nanoparticles were observed on the tips of the VACNFs, which indicated that the coating time was not long enough so only the tips were clearly coated. With 300 mTorr and 60 min coating time, a much better $TiO_2$ nanoparticle coating was obtained in Figure 4.2c, the walls of VACNFs were coated. Figure 4.2d shows the coating at the condition of 300 mTorr and 90 min coating time. In Figure 4.2e, which 300 mTorr and 120 min coating time was used, very nice and tightly packed $TiO_2$ nanoparticles were formed on the walls of VACNFs. In Figure 4.2f, a high partial pressure (600 mTorr) with a shorter time (60 min) was tried. However, it is noted that the scale bar is 5 μm compared to other images with 500 nm, indicating that the amount of precursor was too big and the deposited $TiO_2$ buried the VACNFs and started to form merged bundles. As a result, 300 mTorr and 120 min was concluded as the MOCVD condition for the further study.

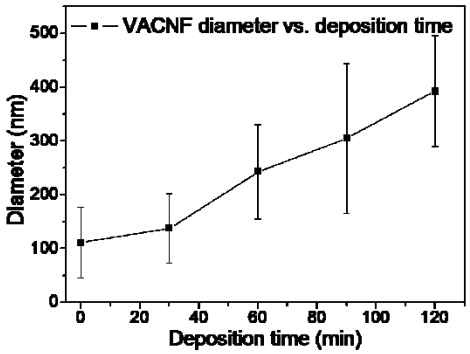


**Figure 4.3. Diameter of $TiO_2$ coated VACNFs under 300 mTorr vs. MOCVD deposition time.**

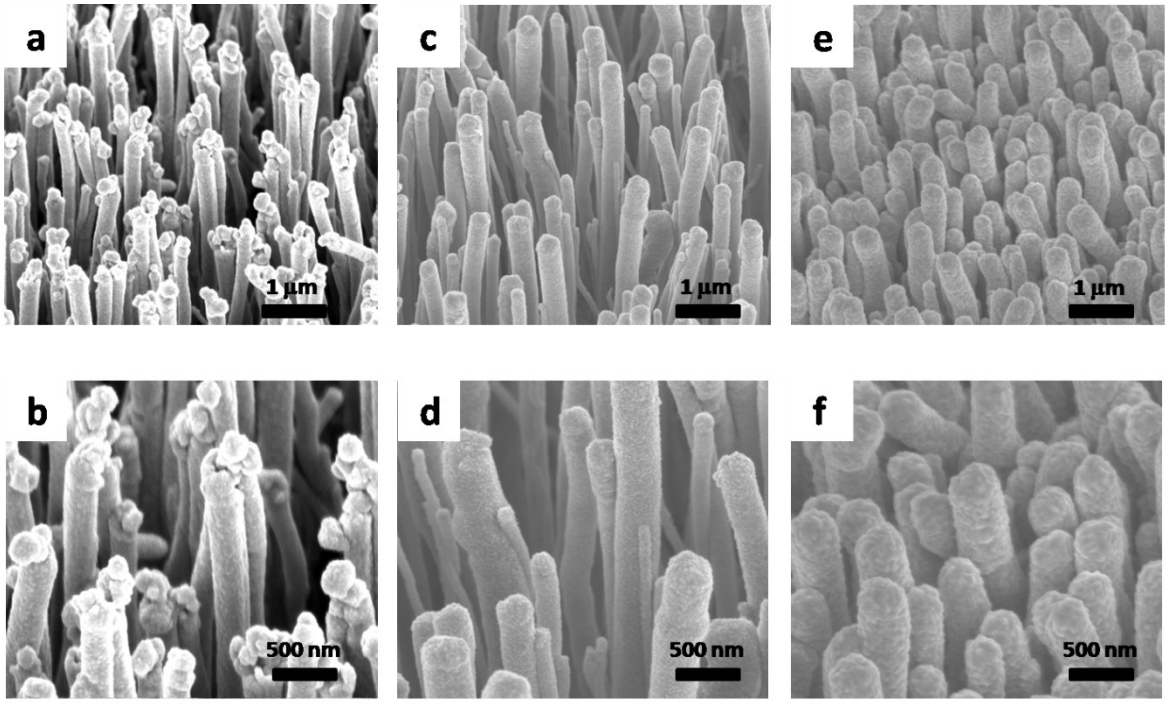


**Figure 4.4. 45°perspective view of SEM images of $TiO_2$ coating using MOCVD process on the as-grown VACNFs under 300 mTorr 120 min condition on (a, b) FTO coated quartz substrate with diameter of about 300 nm, (c, d) Cu substrate with diameter of about 400 nm, (e, f) Si substrate with diameter of about 400 nm.**

After finding the optimal MOCVD condition, VACNFs grown on different substrates were deposited with $TiO_2$ using MOCVD under 300 mTorr for 120 min. SEM images are shown in Figure 4.3, (a, b) are the images of the sample with FTO coated quartz, compared to the images in Figure 4.1a and 4.1b, the diameter of each coated fiber was increased a lot, which was due to that the VACNFs formed bundles during MOCVD process. So each fiber shown in the image is actually a bundle of several fibers, and it was confirmed with the TEM images in Figure 4.3a and 4.3b. Figure 4.3c, 4.3d are the SEM images of $TiO_2$ coated VACNFs on Cu, 4.3e and 4.3f are images of $TiO_2$ coated VACNFs on Si. They both showed good uniformity of the $TiO_2$ coating.

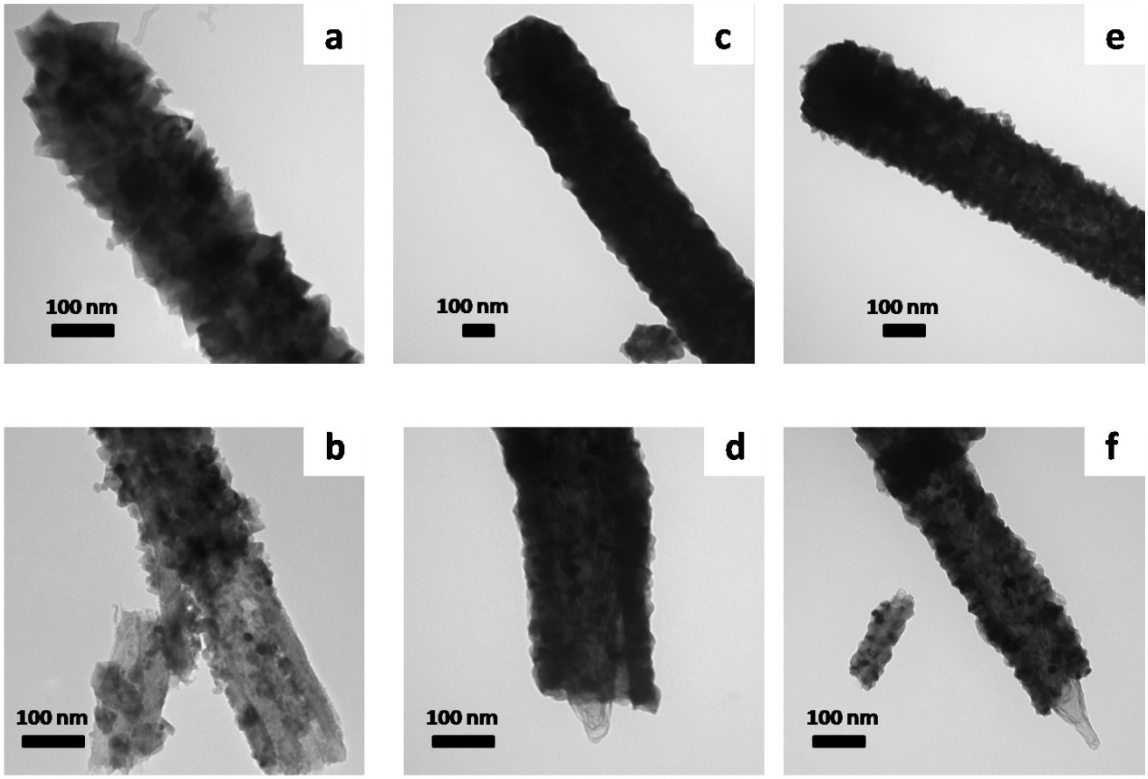


**Figure 4.5. TEM images of $TiO_2$ coating on the as grown VACNFs on (a, b) FTO coated quartz substrate, (c, d) Cu substrate, (e, f) Si substrate.**

TEM characterization was carried out to study MOCVD $TiO_2$ coating around the VACNFs. As mentioned, VACNFs grown on FTO-coated quartz substrate formed bundles during MOCVD process, which resulted in the increased diameter of each fiber shown in the SEM images. Figure 4.4a and 4.4b show the TEM images of $TiO_2$ coated VACNFs on FTO coated quartz. Compared to the VACNFs grown on the other two substrates shown in Figure 4.4c-4.4f, the $TiO_2$ nanoparticles in Figure 4.4a are not as tightly packed as what are shown in the 4.4c-4.4f. The reason why it formed loose packed $TiO_2$ nanoparticles is because the VACNF bundles formed during MOCVD process, which can be seen in Figure 4.4b, which is the bottom of one coated fiber. Many smaller VACNFs with much smaller diameters were observed, which is consistent with what was observed in the SEM images in Figure 4.1a and 4.1b. Figure 4.4c and 4.4d are the TEM images of $TiO_2$ coating on the VACNFs grown on Cu, and the ones on Si are shown in Figure 4.4e and 4.4f. Both show very uniform and well packed $TiO_2$ nanoparticle coating around the VACNFs.

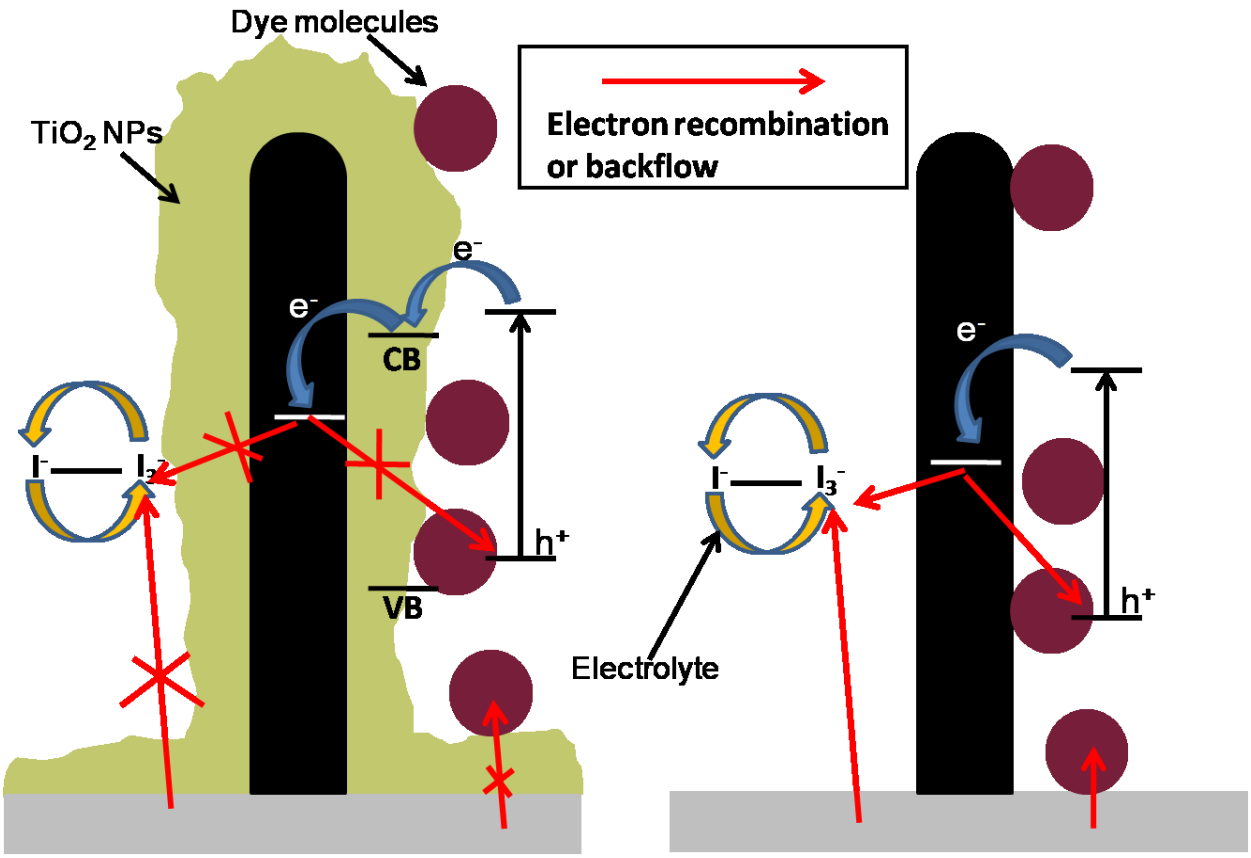


**Scheme 4. Comparison of $TiO_2$ coated VACNFs and non-$TiO_2$ coated VACNFs and the electron transfer, electron recombination and electron backflow routines**

The $TiO_2$ coated VACNFs grown on the FTO coated quarts substrate can be used as a new photoanode structure base for the DSSC system. Schematic 4 shows the structure detail and the electron transfer routine in the DSSC system using $TiO_2$ coated VACNFs as photoanode. The VACNF core provides an "electron highway" on which the electron from the dye molecules can travel much faster than the traditional mesoporous $TiO_2$ nanoparticle network. In the tradition $TiO_2$ nanoparticle network, each $TiO_2$ nanoparticle is attached to each other, the electron injected from dye molecule needs to travel from one $TiO_2$ nanoparticle to another one and finally get to the electrode surface by going through thousands of $TiO_2$ nanoparticles. During the electron transfer through the $TiO_2$ nanoparticle network, because $TiO_2$ is a semiconducting material, a lot of electron traps and electron back flow will happen, which will limit the electron transfer rate. By using the VACNF core, the electron can easily travel within the same fiber without jumping from one particle to another, which effectively improves the electron transfer in the DSSC

system. Moreover, with the $TiO_2$ nanoparticle coating around the VACNFs, the electron recombination and electron flow can be minimized due to the barrier layer effect of the $TiO_2$ coating. With this photoanode base, further study can be carried out based on this structure to make more efficient DSSCs. With the unique property of the $TiO_2$ nanoparticle, this structure can also be used to make the anode in the Lithium ion battery study with a faster charging and discharging rate and a better stability.

## Conclusion

In summary, fabrication of VACNFs on three different substrates were demonstrated, the condition for using MOCVD to coat $TiO_2$ on as grown VACNFs on different substrates were calibrated with an optimal condition with a partial pressure of 300 mTorr and deposition time of 120 min . With too less partial pressure or too short time, there were only small amount or nothing deposited on the VACNSs; with too high partial pressure, the deposition rate was too fast to uniformly coat each single VACNF, instead VACNFs were buried and big crystalline structures were formed. VACNFs grown on FTO coated quartz substrate were found to have smaller diameter than the ones grown on Cu or Si due to low growth temperature (550°C). Because of the small diameter, VACNFs formed bundle structure after MOCVD process, while the other two samples were coated uniformly. $TiO_2$ coated VACNF photoanode has a very large electrode surface area, very good electric conductivity due to VACNF core and minimum electron recombination and back flow, so it can be used as a good base for further studies in DSSCs and Lithium ion batteries.

# Chapter 5 - Overall Conclusion and Future Outlook

In conclusion, properties of the $TiO_2$ barrier layer were systemically studied; two approaches can be used in different DSSC studies. The $TiCl_4$ treatment can be used to create a barrier layer, which minimize the electron recombination and back flow to optimize the DSSC condition, so that a optimized DSSC base can be used in the further DSSC studies. The Ti sputtering method can be used to create a compact blocking layer, which can be used in the DSSC studies, where a smooth and compact substrate is needed.

For the counter electrode study, a new VACNF counter electrode was used to replace the traditional Pt counter electrode to reduce the cost and at the mean time, maintain the performance and stability. With a VACNF counter electrode, a larger electrode surface area was obtained, and with the big amount of active graphitic edges, the redox reaction rate and the catalytic activities can be improved.

Fabrication of VACNFs on different substrates was also studied. FTO coated quartz, Cu and Si were used as substrates to grow VACNFs on them. The VACNFs grown on FTO coated quartz had much smaller diameter than the ones grown on the other two substrates, and that was due to the low growth temperature used for FTO coated quartz substrate to prevent the FTO from degrading. MOCVD process was carried to coat the VACNFs on different substrates with $TiO_2$ layer. The optimal MOCVD condition was found to be 300 mTorr and 120 min under 550 °C. SEM and TEM characterization were carried out to characterize the as grown VACNFs. $TiO_2$ coated VACNFs grown on FTO coated quartz substrate can be used as a new photoanode base in the DSSC system to obtain a faster electron transfer rate with the highly conductive VACNF core. And with the $TiO_2$ coating, which can be served as a barrier layer, the electron recombination and back flow ware minimized. This structure can also be used in the study of Lithium ion batteries.

Overall, an optimized DSSC base was prepared by applying $TiO_2$ barrier layer to suppress the electron recombination and back flow. A cheap, stable VACNF counter electrode was studied and it can be used as a comparable replacement for the traditional Pt counter electrode while maintain the cell performance. A new $TiO_2$ coated VACNF structure was introduced by PECVD and MOCVD processes. The as grown $TiO_2$ coated VACNFs can be used as a new DSSC base with faster electron transfer and minimal electron recombination and back flow for

the future DSSC studies, and such structure can also be used for Lithium ion batteries studies. By combining these three components, a cheap, stable and efficient DSSC system can be obtained.

# References


1. van-Bavel, S. S.; Sourty, E.; Loos, J., Three-dimensional nanoscale organization of bulk heterojunction polymer solar cells. *Nano letters* **2009,** *9* (2), 507-513.
2. Brabec, C. J.; Sariciftci, N. S.; Hummelen, J. C., Plastic solar cells. *Advanced Functional Materials* **2001,** *11* (1), 15-26.
3. Huynh, W. U.; Dittmer, J. J.; Alivisatos, A. P., Hybrid nanorod-polymer solar cells. *science* **2002,** *295* (5564), 2425-2427.
4. Peumans, P.; Uchida, S.; Forrest, S. R., Efficient bulk heterojunction photovoltaic cells using small-molecular-weight organic thin films. *Nature* **2003,** *425* (6954), 158-162.
5. Peumans, P.; Yakimov, A.; Forrest, S. R., Small molecular weight organic thin-film photodetectors and solar cells. *Journal of Applied Physics* **2003,** *93* (7), 3693-3723.
6. Veenstra, S. C.; Loos, J.; Kroon, J. M., Nanoscale structure of solar cells based on pure conjugated polymer blends. *Progress in Photovoltaics: Research and Applications* **2007,** *15* (8), 727-740.
7. Po, R.; Maggini, M.; Camaioni, N., Polymer solar cells: recent approaches and achievements. *The Journal of Physical Chemistry C* **2009,** *114* (2), 695-706.
8. Conibeer, G., Third-generation photovoltaics. *Materials today* **2007,** *10* (11), 42-50.
9. Green, M. A., Third generation photovoltaics: Ultra‐high conversion efficiency at low cost. *Progress in Photovoltaics: Research and Applications* **2001,** *9* (2), 123-135.
10. Kim, J. Y.; Lee, K.; Coates, N. E.; Moses, D.; Nguyen, T.-Q.; Dante, M.; Heeger, A. J., Efficient tandem polymer solar cells fabricated by all-solution processing. *Science* **2007,** *317* (5835), 222-225.
11. Liska, P.; Thampi, K.; Gratzel, M.; Bremaud, D.; Rudmann, D.; Upadhyaya, H.; Tiwari, A., Nanocrystalline dye-sensitized solar cell/copper indium gallium selenide thin-film tandem showing greater than 15% conversion efficiency. *Applied physics letters* **2006,** *88* (20), 203103-203103.
12. Ito, S.; Murakami, T. N.; Comte, P.; Liska, P.; Grätzel, C.; Nazeeruddin, M. K.; Grätzel, M., Fabrication of thin film dye sensitized solar cells with solar to electric power conversion efficiency over 10%. *Thin Solid Films* **2008,** *516* (14), 4613-4619.
13. Kroon, J.; Bakker, N.; Smit, H.; Liska, P.; Thampi, K.; Wang, P.; Zakeeruddin, S.; Grätzel, M.; Hinsch, A.; Hore, S., Nanocrystalline dye‐sensitized solar cells having maximum performance. *Progress in Photovoltaics: Research and Applications* **2007,** *15* (1), 1-18.
14. Martinson, A. B.; Hamann, T. W.; Pellin, M. J.; Hupp, J. T., New Architectures for Dye‐Sensitized Solar Cells. *Chemistry-A European Journal* **2008,** *14* (15), 4458-4467.
15. Arango, A. C.; Oertel, D. C.; Xu, Y.; Bawendi, M. G.; Bulovic, V., Heterojunction photovoltaics using printed colloidal quantum dots as a photosensitive layer. *Nano letters* **2009,** *9* (2), 860-863.
16. Kongkanand, A.; Tvrdy, K.; Takechi, K.; Kuno, M.; Kamat, P. V., Quantum dot solar cells. Tuning photoresponse through size and shape control of CdSe-$TiO_2$ architecture. *Journal of the American Chemical Society* **2008,** *130* (12), 4007-4015.
17. Lee, H. J.; Yum, J.-H.; Leventis, H. C.; Zakeeruddin, S. M.; Haque, S. A.; Chen, P.; Seok, S. I.; Grätzel, M.; Nazeeruddin, M. K., CdSe quantum dot-sensitized solar cells exceeding efficiency 1% at full-sun intensity. *The Journal of Physical Chemistry C* **2008,** *112* (30), 11600-11608.

18. Nozik, A., Quantum dot solar cells. *Physica E: Low-dimensional Systems and Nanostructures* **2002,** *14* (1), 115-120.
19. Lai, Y.-H.; Lin, C.-Y.; Chen, H.-W.; Chen, J.-G.; Kung, C.-W.; Vittal, R.; Ho, K.-C., Fabrication of a ZnO film with a mosaic structure for a high efficient dye-sensitized solar cell. *Journal of Materials Chemistry* **2010,** *20* (42), 9379-9385.
20. Sauvage, F.; Di Fonzo, F.; Li Bassi, A.; Casari, C.; Russo, V.; Divitini, G.; Ducati, C.; Bottani, C.; Comte, P.; Graetzel, M., Hierarchical TiO2 photoanode for dye-sensitized solar cells. *Nano letters* **2010,** *10* (7), 2562-2567.
21. Bukowski, T. J.; Simmons, J. H., Quantum dot research: current state and future prospects. *Critical Reviews in Solid State and Material Sciences* **2002,** *27* (3-4), 119-142.
22. Buonsanti, R.; Carlino, E.; Giannini, C.; Altamura, D.; De Marco, L.; Giannuzzi, R.; Manca, M.; Gigli, G.; Cozzoli, P. D., Hyperbranched anatase TiO2 nanocrystals: nonaqueous synthesis, growth mechanism, and exploitation in dye-sensitized solar cells. *Journal of the American Chemical Society* **2011,** *133* (47), 19216-19239.
23. Guo, W.; Xu, C.; Wang, X.; Wang, S.; Pan, C.; Lin, C.; Wang, Z. L., Rectangular bunched rutile TiO2 nanorod arrays grown on carbon fiber for dye-sensitized solar cells. *Journal of the American Chemical Society* **2012,** *134* (9), 4437-4441.
24. Chandiran, A. K.; Comte, P.; Humphry‐Baker, R.; Kessler, F.; Yi, C.; Nazeeruddin, M.; Grätzel, M., Evaluating the Critical Thickness of TiO2 Layer on Insulating Mesoporous Templates for Efficient Current Collection in Dye‐Sensitized Solar Cells. *Advanced Functional Materials* **2013,** *23* (21), 2775-2781.
25. Paulose, M.; Shankar, K.; Varghese, O. K.; Mor, G. K.; Grimes, C. A., Application of highly-ordered TiO2 nanotube-arrays in heterojunction dye-sensitized solar cells. *Journal of Physics D: Applied Physics* **2006,** *39* (12), 2498.
26. Roy, P.; Kim, D.; Lee, K.; Spiecker, E.; Schmuki, P., TiO2 nanotubes and their application in dye-sensitized solar cells. *Nanoscale* **2010,** *2* (1), 45-59.
27. Zhu, K.; Neale, N. R.; Miedaner, A.; Frank, A. J., Enhanced charge-collection efficiencies and light scattering in dye-sensitized solar cells using oriented TiO2 nanotubes arrays. *Nano Letters* **2007,** *7* (1), 69-74.
28. Chen, P.-Y.; Dang, X.; Klug, M. T.; Qi, J.; Dorval Courchesne, N. m.-M.; Burpo, F. J.; Fang, N.; Hammond, P. T.; Belcher, A. M., Versatile Three-Dimensional Virus-Based Template for Dye-Sensitized Solar Cells with Improved Electron Transport and Light Harvesting. *ACS nano* **2013,** *7* (8), 6563-6574.
29. Wang, H.; Bai, Y.; Wu, Q.; Zhou, W.; Zhang, H.; Li, J.; Guo, L., Rutile TiO2 nano-branched arrays on FTO for dye-sensitized solar cells. *Physical Chemistry Chemical Physics* **2011,** *13* (15), 7008-7013.
30. Du Pasquier, A.; Chen, H.; Lu, Y., Dye sensitized solar cells using well-aligned zinc oxide nanotip arrays. *Applied physics letters* **2006,** *89* (25), 253513.
31. Hsu, Y.; Xi, Y.; Djurišić, A.; Chan, W., ZnO nanorods for solar cells: hydrothermal growth versus vapor deposition. *Applied Physics Letters* **2008,** *92* (13), 133507.
32. Yang, Z.; Xu, T.; Ito, Y.; Welp, U.; Kwok, W. K., Enhanced electron transport in dye-sensitized solar cells using short ZnO nanotips on a rough metal anode. *The Journal of Physical Chemistry C* **2009,** *113* (47), 20521-20526.
33. Zhang, Q.; Zhang, Y.; Huang, S.; Huang, X.; Luo, Y.; Meng, Q.; Li, D., Application of carbon counterelectrode on CdS quantum dot-sensitized solar cells (QDSSCs). *Electrochemistry Communications* **2010,** *12* (2), 327-330.

34. Lee, W. J.; Ramasamy, E.; Lee, D. Y.; Song, J. S., Efficient dye-sensitized solar cells with catalytic multiwall carbon nanotube counter electrodes. *ACS applied materials & interfaces* **2009,** *1* (6), 1145-1149.
35. Park, S.-H.; Jung, H.-R.; Kim, B.-K.; Lee, W.-J., MWCNT/mesoporous carbon nanofibers composites prepared by electrospinning and silica template as counter electrodes for dye-sensitized solar cells. *Journal of Photochemistry and Photobiology A: Chemistry* **2012,** *246*, 45-49.
36. Jiang, W.; Yin, L.; Liu, H.; Ding, Y., Nanograss-structured counter electrode for dye-sensitized solar cells. *Journal of Power Sources* **2012,** *218*, 405-411.
37. Suzuki, K.; Yamaguchi, M.; Kumagai, M.; Yanagida, S., Application of carbon nanotubes to counter electrodes of dye-sensitized solar cells. *Chemistry Letters* **2003,** *32* (1), 28-29.
38. Fan, S.-Q.; Fang, B.; Kim, J. H.; Kim, J.-J.; Yu, J.-S.; Ko, J., Hierarchical nanostructured spherical carbon with hollow core/mesoporous shell as a highly efficient counter electrode in CdSe quantum-dot-sensitized solar cells. *Applied Physics Letters* **2010,** *96* (6), 063501.
39. Fang, B.; Kim, M.; Fan, S.-Q.; Kim, J. H.; Wilkinson, D. P.; Ko, J.; Yu, J.-S., Facile synthesis of open mesoporous carbon nanofibers with tailored nanostructure as a highly efficient counter electrode in CdSe quantum-dot-sensitized solar cells. *Journal of Materials Chemistry* **2011,** *21* (24), 8742-8748.
40. Fang, B.; Fan, S.-Q.; Kim, J. H.; Kim, M.-S.; Kim, M.; Chaudhari, N. K.; Ko, J.; Yu, J.-S., Incorporating hierarchical nanostructured carbon counter electrode into metal-free organic dye-sensitized solar cell. *Langmuir* **2010,** *26* (13), 11238-11243.
41. Sayer, R. A.; Hodson, S. L.; Fisher, T. S., Improved efficiency of dye-sensitized solar cells using a vertically aligned carbon nanotube counter electrode. *Journal of Solar Energy Engineering* **2010,** *132* (2), 021007.
42. Wang, G.; Huang, C.; Xing, W.; Zhuo, S., Micro–meso hierarchical porous carbon as low-cost counter electrode for dye-sensitized solar cells. *Electrochimica Acta* **2011,** *56* (16), 5459-5463.
43. Snaith, H. J.; Karthikeyan, C.; Petrozza, A.; Teuscher, J.; Moser, J. E.; Nazeeruddin, M. K.; Thelakkat, M.; Grätzel, M., High extinction coefficient "Antenna" dye in solid-state dye-sensitized solar cells: a photophysical and electronic study. *The Journal of Physical Chemistry C* **2008,** *112* (20), 7562-7566.
44. Kim, S.; Lee, J. K.; Kang, S. O.; Ko, J.; Yum, J.-H.; Fantacci, S.; De Angelis, F.; Di Censo, D.; Nazeeruddin, M. K.; Grätzel, M., Molecular engineering of organic sensitizers for solar cell applications. *Journal of the American Chemical Society* **2006,** *128* (51), 16701-16707.
45. Gao, F.; Wang, Y.; Shi, D.; Zhang, J.; Wang, M.; Jing, X.; Humphry-Baker, R.; Wang, P.; Zakeeruddin, S. M.; Grätzel, M., Enhance the optical absorptivity of nanocrystalline TiO2 film with high molar extinction coefficient ruthenium sensitizers for high performance dye-sensitized solar cells. *Journal of the American Chemical Society* **2008,** *130* (32), 10720-10728.
46. Campbell, W. M.; Jolley, K. W.; Wagner, P.; Wagner, K.; Walsh, P. J.; Gordon, K. C.; Schmidt-Mende, L.; Nazeeruddin, M. K.; Wang, Q.; Grätzel, M., Highly efficient porphyrin sensitizers for dye-sensitized solar cells. *The Journal of Physical Chemistry C* **2007,** *111* (32), 11760-11762.
47. Kuang, D.; Ito, S.; Wenger, B.; Klein, C.; Moser, J.-E.; Humphry-Baker, R.; Zakeeruddin, S. M.; Grätzel, M., High molar extinction coefficient heteroleptic ruthenium complexes for

thin film dye-sensitized solar cells. *Journal of the American Chemical Society* **2006,** *128* (12), 4146-4154.
48. Schmidt‐Mende, L.; Bach, U.; Humphry‐Baker, R.; Horiuchi, T.; Miura, H.; Ito, S.; Uchida, S.; Grätzel, M., Organic Dye for Highly Efficient Solid‐State Dye‐Sensitized Solar Cells. *Advanced Materials* **2005,** *17* (7), 813-815.
49. Nazeeruddin, M. K.; Klein, C.; Liska, P.; Grätzel, M., Synthesis of novel ruthenium sensitizers and their application in dye-sensitized solar cells. *Coordination chemistry reviews* **2005,** *249* (13), 1460-1467.
50. O'regan, B.; Grfitzeli, M., A low-cost, high-efficiency solar cell based on dye-sensitized. *Nature* **1991,** *353*, 24.
51. Hart, J. N.; Menzies, D.; Cheng, Y.-B.; Simon, G. P.; Spiccia, L., $TiO_2$ sol–gel blocking layers for dye-sensitized solar cells. *C. R. Chim.* **2006,** *9* (5), 622-626.
52. Hattori, R.; Goto, H., Carrier leakage blocking effect of high temperature sputtered $TiO_2$ film on dye-sensitized mesoporous photoelectrode. *Thin Solid Films* **2007,** *515* (20), 8045-8049.
53. Seo, H.; Son, M.-K.; Kim, J.-K.; Shin, I.; Prabakar, K.; Kim, H.-J., Method for fabricating the compact layer in dye-sensitized solar cells by titanium sputter deposition and acid-treatments. *Sol. Energy Mater. Sol. Cells* **2011,** *95* (1), 340-343.
54. Shi, J.; Liang, J.; Peng, S.; Xu, W.; Pei, J.; Chen, J., Synthesis, characterization and electrochemical properties of a compact titanium dioxide layer. *Solid State Sci.* **2009,** *11* (2), 433-438.
55. Xia, J.; Masaki, N.; Jiang, K.; Yanagida, S., Deposition of a Thin Film of $TiO_x$ from a Titanium Metal Target as Novel Blocking Layers at Conducting Glass/$TiO_2$ Interfaces in Ionic Liquid Mesoscopic $TiO_2$ Dye-Sensitized Solar Cells. *J. Phys. Chem. B* **2006,** *110* (50), 25222-25228.
56. Yu, H.; Zhang, S.; Zhao, H.; Will, G.; Liu, P., An efficient and low-cost $TiO_2$ compact layer for performance improvement of dye-sensitized solar cells. *Electrochim. Acta* **2009,** *54* (4), 1319-1324.
57. Ito, S.; Liska, P.; Comte, P.; Charvet, R.; Pechy, P.; Bach, U.; Schmidt-Mende, L.; Zakeeruddin, S. M.; Kay, A.; Nazeeruddin, M. K.; Gratzel, M., Control of dark current in photoelectrochemical ($TiO_2$/$I^-$-$I_3^-$) and dye-sensitized solar cells. *Chem. Commun.* **2005,** (34), 4351-4353.
58. Burke, A.; Ito, S.; Snaith, H.; Bach, U.; Kwiatkowski, J.; Grätzel, M., The function of a $TiO_2$ compact layer in dye-sensitized solar cells incorporating "planar" organic dyes. *Nano lett.* **2008,** *8* (4), 977-981.
59. Hore, S.; Kern, R., Implication of device functioning due to back reaction of electrons via the conducting glass substrate in dye sensitized solar cells. *Appl. Phys. Lett.* **2005,** *87* (26), -.
60. Krüger, J.; Plass, R.; Grätzel, M.; Cameron, P. J.; Peter, L. M., Charge Transport and Back Reaction in Solid-State Dye-Sensitized Solar Cells: A Study Using Intensity-Modulated Photovoltage and Photocurrent Spectroscopy. *J. Phys. Chem. B* **2003,** *107* (31), 7536-7539.
61. Krüger, J.; Plass, R.; Cevey, L.; Piccirelli, M.; Grätzel, M.; Bach, U., High efficiency solid-state photovoltaic device due to inhibition of interface charge recombination. *Appl. Phys. Lett.* **2001,** *79* (13), 2085-2087.
62. Peng, B.; Jungmann, G.; Jäger, C.; Haarer, D.; Schmidt, H.-W.; Thelakkat, M., Systematic investigation of the role of compact $TiO_2$ layer in solid state dye-sensitized $TiO_2$ solar cells. *Coord. Chem. Rev.* **2004,** *248* (13), 1479-1489.

63. Ahn, K.-S.; Kang, M.-S.; Lee, J.-W.; Kang, Y. S., Effects of a surfactant-templated nanoporous $TiO_2$ interlayer on dye-sensitized solar cells. *J. Appl. Phys.* **2007,** *101* (8), -.
64. Yang, Y.; Jankowiak, R.; Lin, C.; Holzwarth, A.; Li, J., Effect of the LHCII Pigment-Protein Complex Aggregation on Photovoltaic Properties of Sensitized $TiO_2$ Solar Cells. *Phys. Chem. Chem. Phys*, submitted.
65. Mor, G. K.; Shankar, K.; Paulose, M.; Varghese, O. K.; Grimes, C. A., Use of highly-ordered $TiO_2$ nanotube arrays in dye-sensitized solar cells. *Nano Lett.* **2006,** *6* (2), 215-218.
66. Liu, J.; Kuo, Y.-T.; Klabunde, K. J.; Rochford, C.; Wu, J.; Li, J., Novel Dye-Sensitized Solar Cell Architecture Using $TiO_2$-Coated Vertically Aligned Carbon Nanofiber Arrays. *ACS Appl. Mater. Interfaces* **2009,** *1* (8), 1645-1649.
67. Kavan, L.; Grätzel, M., Highly efficient semiconducting $TiO_2$ photoelectrodes prepared by aerosol pyrolysis. *Electrochim. Acta* **1995,** *40* (5), 643-652.
68. Ahn, K.-S.; Kang, M.-S.; Lee, J.-W.; Kang, Y. S., Effects of a surfactant-templated nanoporous TiO2 interlayer on dye-sensitized solar cells. *Journal of applied physics* **2007,** *101* (8), 084312.
69. Hart, J. N.; Menzies, D.; Cheng, Y.-B.; Simon, G. P.; Spiccia, L., TiO< sub> 2</sub> sol–gel blocking layers for dye-sensitized solar cells. *Comptes Rendus Chimie* **2006,** *9* (5), 622-626.
70. Bisquert, J.; Fabregat-Santiago, F.; Mora-Sero, I.; Garcia-Belmonte, G.; Gimenez, S., Electron Lifetime in Dye-Sensitized Solar Cells: Theory and Interpretation of Measurements. *J. Phys. Chem. C* **2009,** *113* (40), 17278-17290.
71. Vesce, L.; Riccitelli, R.; Soscia, G.; Brown, T. M.; Di Carlo, A.; Reale, A., Optimization of nanostructured titania photoanodes for dye-sensitized solar cells: Study and experimentation of $TiCl_4$ treatment. *J. Non-Cryst. Solids* **2010,** *356* (37), 1958-1961.
72. Lindstrom, H.; Sodergren, S.; Solbrand, A.; Rensmo, H.; Hjelm, J.; Hagfeldt, A.; Lindquist, S. E., $Li^+$ ion insertion in $TiO_2$ (anatase) .2. Voltammetry on nanoporous films. *J. Phys. Chem. B* **1997,** *101* (39), 7717-7722.
73. Zaban, A.; Greenshtein, M.; Bisquert, J., Determination of the Electron Lifetime in Nanocrystalline Dye Solar Cells by Open Circuit Voltage Decay Measurements. *Chem. Phys. Chem* **2003,** *4* (8), 859-864.
74. Zhu, K.; Neale, N. R.; Halverson, A. F.; Kim, J. Y.; Frank, A. J., Effects of Annealing Temperature on the Charge-Collection and Light-Harvesting Properties of $TiO_2$ Nanotube-Based Dye-Sensitized Solar Cells. *J. Phys. Chem. C* **2010,** *114* (32), 13433-13441.
75. Zhang, J.; Li, M.; Feng, Z.; Chen, J.; Li, C., UV Raman spectroscopic study on $TiO_2$. I. Phase transformation at the surface and in the bulk. *J. Phys. Chem. B* **2006,** *110* (2), 927-935.
76. Fan, B.; Mei, X.; Sun, K.; Ouyang, J., Conducting polymer/carbon nanotube composite as counter electrode of dye-sensitized solar cells. *Applied Physics Letters* **2008,** *93* (14), 143103.
77. Huang, K.-C.; Wang, Y.-C.; Dong, R.-X.; Tsai, W.-C.; Tsai, K.-W.; Wang, C.-C.; Chen, Y.-H.; Vittal, R.; Lin, J.-J.; Ho, K.-C., A high performance dye-sensitized solar cell with a novel nanocomposite film of PtNP/MWCNT on the counter electrode. *Journal of Materials Chemistry* **2010,** *20* (20), 4067-4073.
78. Cha, S. I.; Koo, B.; Seo, S.; Lee, D. Y., Pt-free transparent counter electrodes for dye-sensitized solar cells prepared from carbon nanotube micro-balls. *J. Mater. Chem.* **2010,** *20* (4), 659-662.

79. Lin, J.-Y.; Liao, J.-H.; Hung, T.-Y., A composite counter electrode of CoS/MWCNT with high electrocatalytic activity for dye-sensitized solar cells. *Electrochemistry Communications* **2011,** *13* (9), 977-980.
80. Xiao, Y.; Wu, J.; Yue, G.; Lin, J.; Huang, M.; Lan, Z., Low temperature preparation of a high performance Pt/SWCNT counter electrode for flexible dye-sensitized solar cells. *Electrochimica Acta* **2011,** *56* (24), 8545-8550.
81. Uk Lee, S.; Seok Choi, W.; Hong, B., A comparative study of dye-sensitized solar cells added carbon nanotubes to electrolyte and counter electrodes. *Solar Energy Materials and Solar Cells* **2010,** *94* (4), 680-685.
82. Zhu, H.; Zeng, H.; Subramanian, V.; Masarapu, C.; Hung, K.-H.; Wei, B., Anthocyanin-sensitized solar cells using carbon nanotube films as counter electrodes. *Nanotechnology* **2008,** *19* (46), 465204.
83. Calogero, G.; Bonaccorso, F.; Maragò, O. M.; Gucciardi, P. G.; Di Marco, G., Single wall carbon nanotubes deposited on stainless steel sheet substrates as novel counter electrodes for ruthenium polypyridine based dye sensitized solar cells. *Dalton Transactions* **2010,** *39* (11), 2903-2909.
84. Joshi, P.; Zhang, L.; Chen, Q.; Galipeau, D.; Fong, H.; Qiao, Q., Electrospun carbon nanofibers as low-cost counter electrode for dye-sensitized solar cells. *ACS applied materials & interfaces* **2010,** *2* (12), 3572-3577.
85. Chen, J.; Li, B.; Zheng, J.; Zhao, J.; Jing, H.; Zhu, Z., Polyaniline nanofiber/carbon film as flexible counter electrodes in platinum-free dye-sensitized solar cells. *Electrochimica Acta* **2011,** *56* (12), 4624-4630.
86. Hou, S.; Cai, X.; Fu, Y.; Lv, Z.; Wang, D.; Wu, H.; Zhang, C.; Chu, Z.; Zou, D., Transparent conductive oxide-less, flexible, and highly efficient dye-sensitized solar cells with commercialized carbon fiber as the counter electrode. *J. Mater. Chem.* **2011,** *21* (36), 13776-13779.
87. Velten, J.; Mozer, A. J.; Li, D.; Officer, D.; Wallace, G.; Baughman, R.; Zakhidov, A., Carbon nanotube/graphene nanocomposite as efficient counter electrodes in dye-sensitized solar cells. *Nanotechnology* **2012,** *23* (8), 085201.
88. Hong, W.; Xu, Y.; Lu, G.; Li, C.; Shi, G., Transparent graphene/PEDOT–PSS composite films as counter electrodes of dye-sensitized solar cells. *Electrochemistry Communications* **2008,** *10* (10), 1555-1558.
89. Roy-Mayhew, J. D.; Bozym, D. J.; Punckt, C.; Aksay, I. A., Functionalized graphene as a catalytic counter electrode in dye-sensitized solar cells. *Acs Nano* **2010,** *4* (10), 6203-6211.
90. Choi, H.; Kim, H.; Hwang, S.; Han, Y.; Jeon, M., Graphene counter electrodes for dye-sensitized solar cells prepared by electrophoretic deposition. *Journal of Materials Chemistry* **2011,** *21* (21), 7548-7551.
91. Choi, H.; Kim, H.; Hwang, S.; Choi, W.; Jeon, M., Dye-sensitized solar cells using graphene-based carbon nano composite as counter electrode. *Solar Energy Materials and Solar Cells* **2011,** *95* (1), 323-325.
92. Zhang, D.; Li, X.; Li, H.; Chen, S.; Sun, Z.; Yin, X.; Huang, S., Graphene-based counter electrode for dye-sensitized solar cells. *Carbon* **2011,** *49* (15), 5382-5388.
93. Ngo, Q.; Yamada, T.; Suzuki, M.; Ominami, Y.; Cassell, A. M.; Li, J.; Meyyappan, M.; Yang, C. Y., Structural and electrical characterization of carbon nanofibers for interconnect via applications. *Nanotechnology, IEEE Transactions on* **2007,** *6* (6), 688-695.

94. Melechko, A. V.; Merkulov, V. I.; McKnight, T. E.; Guillorn, M.; Klein, K. L.; Lowndes, D. H.; Simpson, M. L., Vertically aligned carbon nanofibers and related structures: controlled synthesis and directed assembly. *Journal of applied physics* **2005,** *97* (4), 041301.
95. Sun, H.; Luo, Y.; Zhang, Y.; Li, D.; Yu, Z.; Li, K.; Meng, Q., In situ preparation of a flexible polyaniline/carbon composite counter electrode and its application in dye-sensitized solar cells. *The Journal of Physical Chemistry C* **2010,** *114* (26), 11673-11679.
96. Nugent, J.; Santhanam, K.; Rubio, A.; Ajayan, P., Fast electron transfer kinetics on multiwalled carbon nanotube microbundle electrodes. *Nano Letters* **2001,** *1* (2), 87-91.
97. Banks, C. E.; Davies, T. J.; Wildgoose, G. G.; Compton, R. G., Electrocatalysis at graphite and carbon nanotube modified electrodes: edge-plane sites and tube ends are the reactive sites. *Chemical Communications* **2005,** (7), 829-841.
98. Šljukic, B.; Banks, C. E.; Compton, R. G., Iron oxide particles are the active sites for hydrogen peroxide sensing at multiwalled carbon nanotube modified electrodes. *Nano letters* **2006,** *6* (7), 1556-1558.
99. Tian, H.; Hu, L.; Li, W.; Sheng, J.; Xu, S.; Dai, S., A facile synthesis of anatase N, B codoped TiO2 anodes for improved-performance dye-sensitized solar cells. *Journal of Materials Chemistry* **2011,** *21* (20), 7074-7077.
100. Kim, D.; Ghicov, A.; Albu, S. P.; Schmuki, P., Bamboo-type TiO2 nanotubes: improved conversion efficiency in dye-sensitized solar cells. *Journal of the American Chemical Society* **2008,** *130* (49), 16454-16455.
101. Baxter, J. B.; Walker, A.; Van Ommering, K.; Aydil, E., Synthesis and characterization of ZnO nanowires and their integration into dye-sensitized solar cells. *Nanotechnology* **2006,** *17* (11), S304.
102. Baxter, J. B.; Aydil, E. S., Dye-sensitized solar cells based on semiconductor morphologies with ZnO nanowires. *Solar Energy Materials and Solar Cells* **2006,** *90* (5), 607-622.
103. Liu, Z.; Liu, C.; Ya, J.; Lei, E., Controlled synthesis of ZnO and TiO< sub> 2</sub> nanotubes by chemical method and their application in dye-sensitized solar cells. *Renewable Energy* **2011,** *36* (4), 1177-1181.
104. Martinson, A. B.; Elam, J. W.; Hupp, J. T.; Pellin, M. J., ZnO nanotube based dye-sensitized solar cells. *Nano letters* **2007,** *7* (8), 2183-2187.
105. Han, J.; Fan, F.; Xu, C.; Lin, S.; Wei, M.; Duan, X.; Wang, Z. L., ZnO nanotube-based dye-sensitized solar cell and its application in self-powered devices. *Nanotechnology* **2010,** *21* (40), 405203.
106. Yang, N.; Zhai, J.; Wang, D.; Chen, Y.; Jiang, L., Two-dimensional graphene bridges enhanced photoinduced charge transport in dye-sensitized solar cells. *Acs Nano* **2010,** *4* (2), 887-894.
107. Yi, H. M13 virus/single-walled carbon nanotubes as a materials platform for energy devices and biomedical applications. Massachusetts Institute of Technology, 2011.
108. Liu, J.; Li, J.; Sedhain, A.; Lin, J.; Jiang, H., Structure and photoluminescence study of TiO2 nanoneedle texture along vertically aligned carbon nanofiber arrays. *The Journal of Physical Chemistry C* **2008,** *112* (44), 17127-17132.

# Appendix A – Supporting Information for Chapter 2

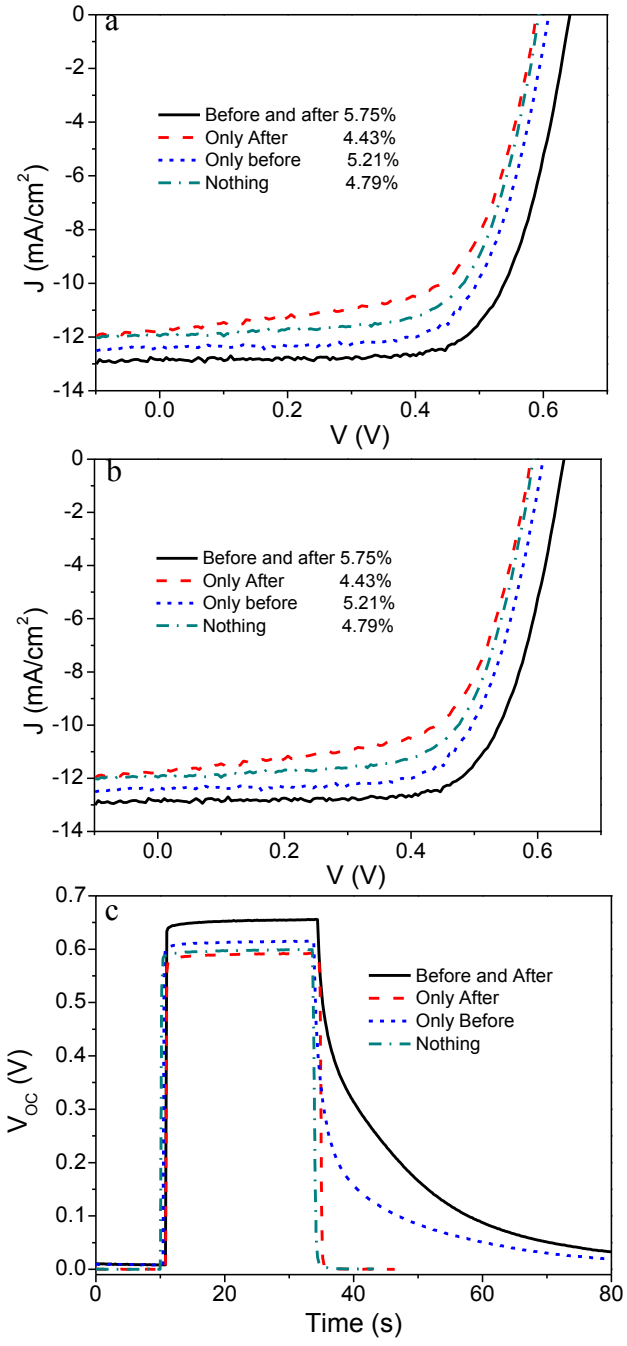


**Figure A1**. The I-V curves of various DSSCs consisting of N719 dye on a ~5 μm thick $TiO_2$ nanoparticle film (a) in dark and (b) under 1 sun illumination through an AM1.5G filter. (c) The response of the open-circuit voltage $V_{OC}$ of these DSSCs as the light was switched on and off.

Four different DSSCs were prepared using the following photoanodes: (1) with a $TiO_2$ barrier layer by 20 min $TiCl_4$ treatment before applying $TiO_2$ nanoparticle paste and followed with a typical 30 min $TiCl_4$ treatment after thermal annealing of the $TiO_2$ nanoparticle film (black line), (2) with only the $TiO_2$ barrier layer before applying the $TiO_2$ nanoparticle paste (green dot-dashed line), (3) only applying the typical 30 min $TiCl_4$ treatment after annealing the $TiO_2$ nanoparticle paste (red dashed line), and (4) without any $TiCl_4$ treatment.

**Experimental details**: All the DSSCs were characterized using a 0.25 $cm^2$ window mask. The DSSC with $TiCl_4$ treatment before and after deposition of the ~5 μm $TiO_2$ nanoparticle film showed the best performance with the largest $J_{SC}$, highest $V_{OC}$, and highest conversion efficiency (see inset of panel b), and smallest $V_{OC}$ decay time constant (i.e. longest photoelectron lifetime). The $TiCl_4$ treatment before applying $TiO_2$ nanoparticle paste is critical in creating a $TiO_2$ barrier between $TiO_2$ nanoparticles and FTO electrode, which minimizes the photoelectron backflow and recombination in the DSSC system. The second $TiCl_4$ treatment post $TiO_2$ nanoparticle film formation is a general procedure in fabrication of Grätzel cells and is commonly believed to improve the physical connection between the $TiO_2$ nanoparticles.

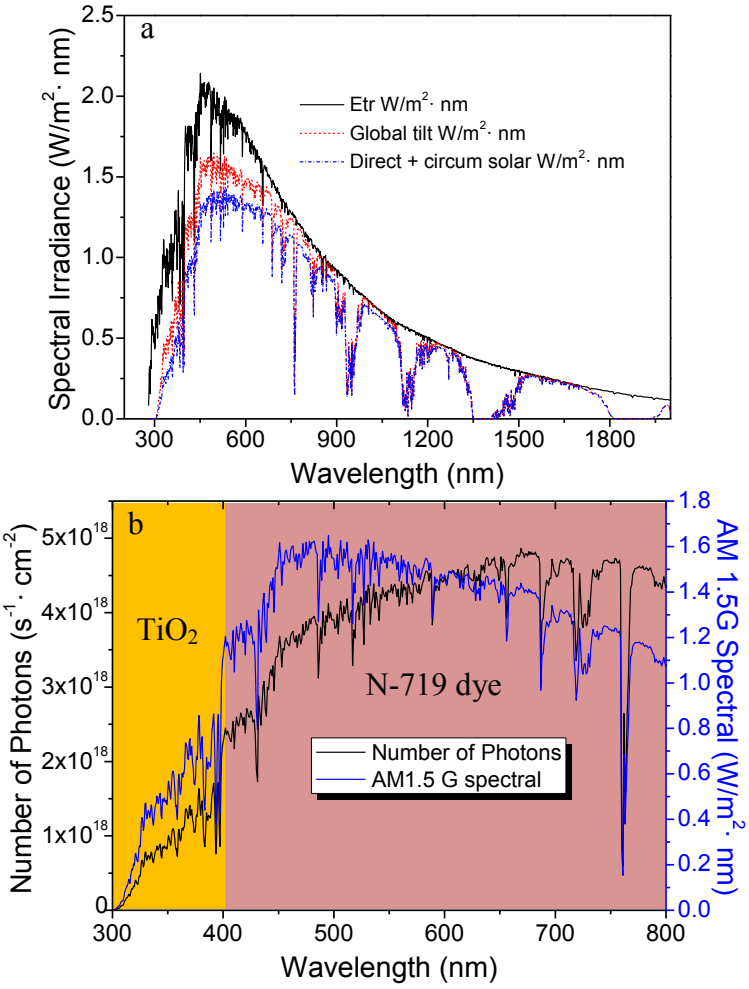


**Figure A2**. (a) The standard solar spectra.(from an online source: http://rredc.nrel.gov/solar/spectra/am1.5/ASTMG173/ASTMG173.html). The 1 sun AM1.5G standard is represented by the red curve. (b) The presentation of the AM1.5G spectrum in irradiance (blue line) and number of photons $N_p$ (black line) vs. the wavelength. The yellow and pink areas under the black curve represent the total incident photons that could be absorbed by the $TiO_2$ barrier layer and N719 dye, respectively.

**Photocurrent estimation**: The contribution to the $J_{SC}$ by photon absorption in the $TiO_2$ barrier layer and the N719 dye can be roughly estimated by the following procedures: (1) converting the AM1.5G solar spectra from irradiance (in unit of W/(m$^2$ nm)) to number of photons $N_p$ (in unit of $s^{-1}cm^{-2}$) by dividing the photon energy $hc/\lambda$; (2) multiplying the IPCE value (shown in Figure 2.2b and 2.2e, respectively) with the average $N_p$ in the same wavelength interval; and (3) taking

the sum of the multiplication product over all wavelength intervals of the IPCE curves. The resulting estimated $J_{SC}$ is ~7.8 μA/cm$^2$ with bare $TiO_2$ barrier layer as the photoanode and ~67 μA/cm$^2$ after sensitized with N719 dye. The approximately ten fold increase is consistent with the large $J_{SC}$ increase from the I-V data in Figure 2.2a to that of Figure 2.2d, indicating that the N719 dye makes the dominant contribution to the photocurrent even though its maximum IPCE is lower than that of $TiO_2$ layer.

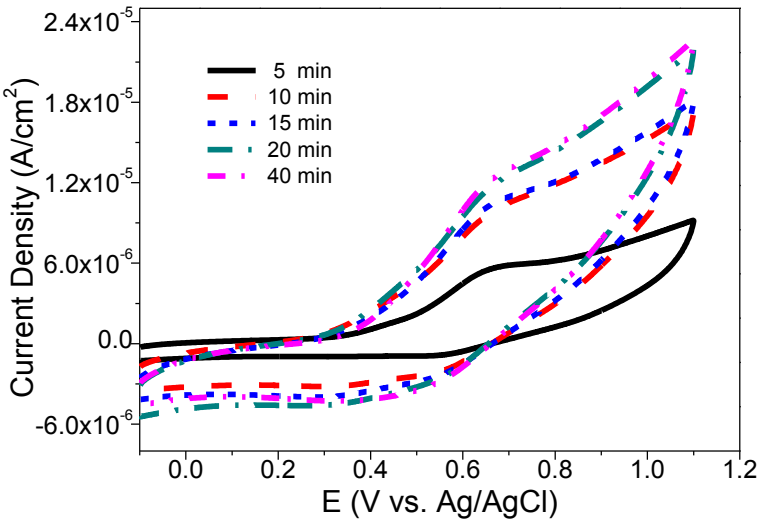


**Figure A3**. Cyclic voltammograms of $TiCl_4$ treated samples. The reference electrode was made of Ag/AgCl in an acetonitrile filling solution containing 10 mM $AgNO_3$ and 1 M $LiClO_4$. The measurements were taken at 50 mV/s scan rate.

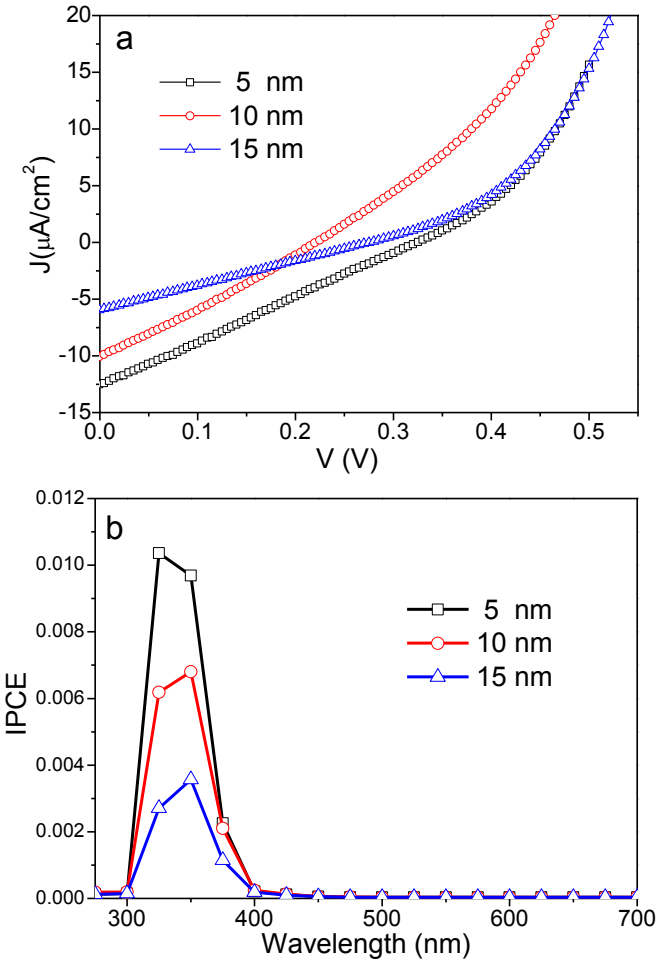


**Figure A4**. Photovoltaic characterization of the control DSSCs without dye sensitizers, which were fabricated with the FTO/glass photoanodes covered with $TiO_2$ barrier layers converted by thermal oxidation of sputtered Ti metal films at different thicknesses: (a) I-V curves under 1 sun AM1.5G illumination and (b) IPCE curves.

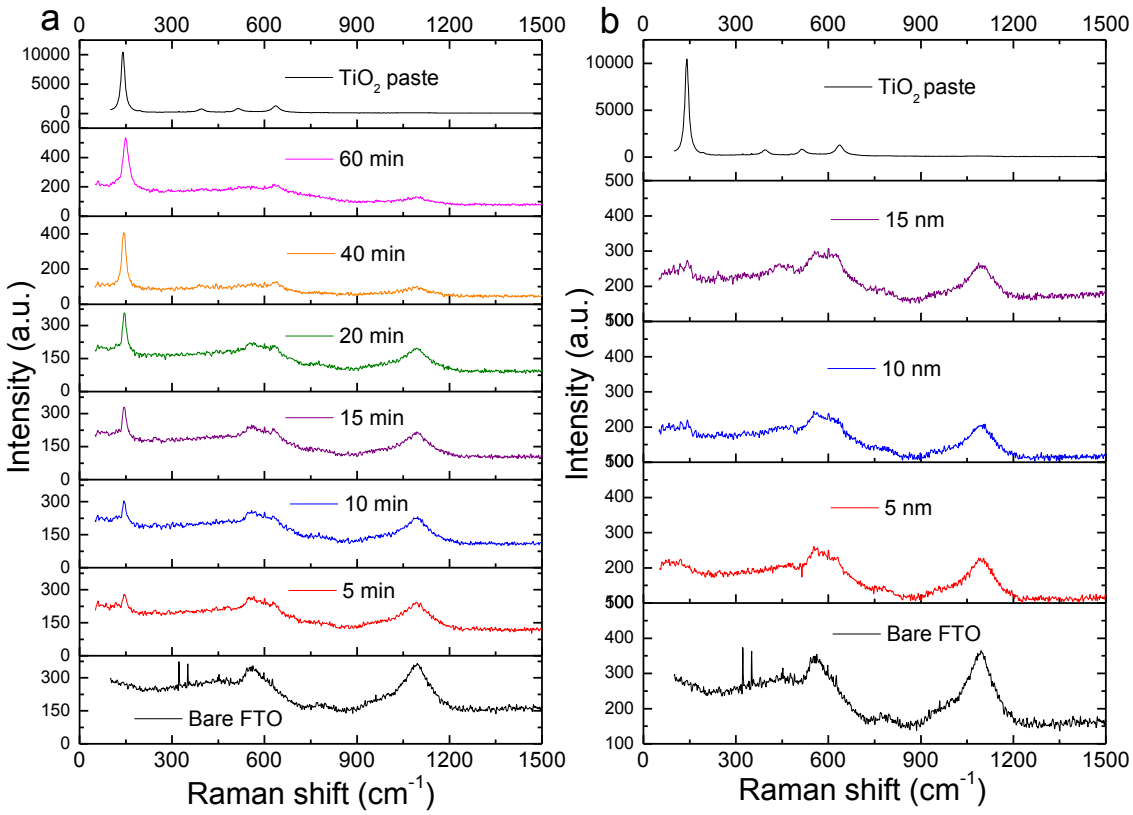


**Figure A5**. Raman spectra of the $TiO_2$ overlayer structure formed by (a) the $TiCl_4$ treatment (0 min to 60 min) and (b) thermal oxidation of sputtered Ti metal films (0 nm to 15 nm). The 20 nm diameter anatase $TiO_2$ nanoparticle paste for DSSC fabrication (Solaronix, Aubonne, Switzerland) were used as a control in the top panels. Anatase structured $TiO_2$ has a large peak at 143 $cm^{-1}$, and three small peaks at 395, 515 and 638 $cm^{-1}$. The bottom panels are the Raman spectrum of bare FTO as a control blank. With increasing $TiCl_4$ treatment time, the peak at 143 $cm^{-1}$ increased as the $TiO_2$ barrier became thicker. In panel b, the intensity of the characteristic anatase feature at 143 $cm^{-1}$ is very weak and comparable to the rutile features at 448 and 610 $cm^{-1}$. It is inconclusive whether it formed anatase, rutile, or amorphous structure.

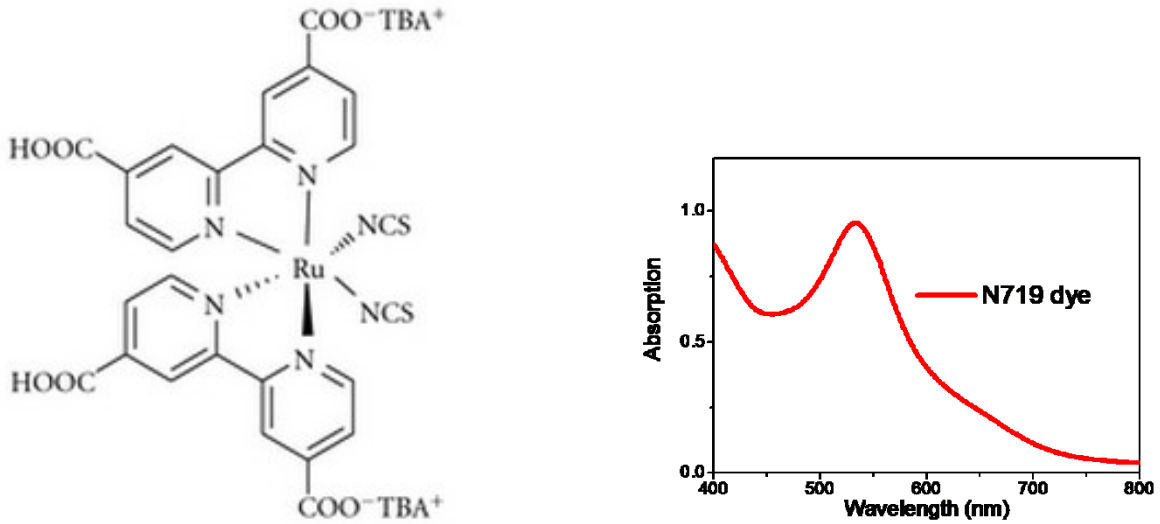


**Figure A6**. Molecular structure and UV-vis absorption spectrum of N-719 dye used in this study.